Available online at www.sciencedirect.com

ScienceDirect

Advances in Space Research xxx (2014) xxx–xxx

ADVANCES IN SPACE RESEARCH (a COSPAR publication)

www.elsevier.com/locate/asr

Mapping of high pressure metamorphics in the As Sifah region, NE Oman using ASTER data

Sankaran Rajendran [a,*], Sobhi Nasir [b]

[a] Department of Earth Sciences, Sultan Qaboos University, Al-Khod, 123 Muscat, Oman
[b] Earth Science Research Centre, Sultan Qaboos University, Al-Khod, 123 Muscat, Oman

Received 11 June 2014; received in revised form 3 November 2014; accepted 25 November 2014

Abstract

The high pressure metamorphic zone of As Sifah area in the Saih Hatat window, NE Oman plays a vital role to study global tectonic setting, metamorphism, transport direction and age of initial ophiolite emplacement. Scientists and researchers are keen in determining the protolith, structural evolution, and timing and metamorphic conditions of the Saih Hatat area. In this study, mapping of the metamorphic zone and discrimination of associated rock formations occurred in the As Sifah region is carried out using visible and near infrared–shortwave infrared (VNIR–SWIR) spectral bands of Advanced Spaceborne Thermal Emission and Reflection Radiometer (ASTER) and well known image processing methods such as image decorrelation, Principal Component Analysis (PCA) and Spectral Angel Mapper (SAM). The study delineated the region of metamorphic zone and discriminated the different metamorphic and carbonate rocks of the study area characterized by hydroxyl (OH) and carbonate bearing minerals. The assessment of accuracy for the occurrence and spatial distribution of major lithological units provided the overall accuracy of 96.06% with Kappa Coefficient = 0.95 in the matrix of Maximum Likelihood (ML) and compared with the Spectral Angle Mapper (SAM) and Spectral Information Divergence (SID) algorithms. The occurrence of such minerals are detected and confirmed by SAM supervised classification method. The study also describes the spectral character of metamorphic and carbonates minerals. The metamorphic zone and associated rock types interpreted over the images are verified in the field and checked for their occurrences and spatial distributions. The occurrence of CO_3 bearing carbonate minerals and OH bearing metamorphic minerals are confirmed further under microscope, XRD analysis and PIMA spectral measurements in the laboratory studies. The study proved sensor capability of ASTER to discriminate metamorphic rocks from associated formations and detection of different mineral occurrences. It is recommended to use the studied technique to map metamorphic zone occurred in the rugged topography, where it is difficult to do conventional geological mapping in similar arid regions.

Keywords: ASTER sensor; High pressure metamorphic zone; Image processing; Spectral properties; As Sifah; Sultanate of Oman

1. Introduction

The Samail ophiolite of Sultanate of Oman is one of the largest thrust sheets on Earth with a length of >400 km, a width of 150 km, and an inferred pre-emplacement thickness of 15–20 km. It is thrust over the adjacent oceanic lithosphere and then onto the Arabian craton with several hundred meter thickness. It has developed a thin sliver of metamorphic rocks comprised high-temperature shear zone called 'metamorphic sole', the first material to underlie the "hot" ophiolite (Searle, 1985). Study on the high pressure metamorphic zones along the Arabian craton is more significant and provoke interest among geologists and scientists to provide key informations to understand the tectonic setting, pressure, temperature, transport direction, and the age of initial ophiolite emplacement. The zone has been described as partially melted amphibolite rocks

* Corresponding author. Tel.: +968 97791859; fax: +968 24413415.
E-mail address: sankaranrajendran@yahoo.com (S. Rajendran).

http://dx.doi.org/10.1016/j.asr.2014.11.026
0273-1177/

grading downward into greenschist facies during the early and intraoceanic thrusting stage of emplacement, where the greenschists are inferred as elastic sediment (Searle and Malpas, 1980, 1982; Pearce et al., 1981; Searle, 1985; Lippard et al., 1986; Goffé et al., 1988; Le Métour et al., 1990; Hanna, 1990; Searle et al., 1994; Gregory et al., 1998; Miller et al., 1998, 1999; Gray et al., 2000). The Saih Hatat window of the northeastern Oman Mountains has undergone intense ductile strain deformation in subduction zone resulted the exhumation of high-pressure in deep level and developed eclogite, garnet blueschist, and carpholite-grade metamorphic rocks and the regions are studied extensively by several workers (e.g. Goffé et al. (1988), Searle et al. (1994, 2004), Searle and Malpas (1980, 1982), Serale and Cox (1999, 2002), El-Shazly et al. (1990, 1994, 1997, 2001), Miller et al. (1998, 2002), Warren and Waters (2006), Yamato et al. (2007), Massonne et al. (2013)). The study on the exhumation of high pressure and low temperature (high P/T) metamorphic rocks has attracted some investigators (Draper and Bone, 1981; Ernst, 1988) to develop several tectonic models and explain metamorphic processes (Cloos, 1986; Davy and Gillet, 1986; Platt, 1986; Avé Lallemant and Guth, 1990; Dobretsov, 1991; Avigad, 1992; Mann and Gordon, 1996). Especially, more scientific attentions were given to the deepest-level As Sifah eclogite and garnet blueschist of the region. The calculated P–T conditions of metamorphism occurred in the As Sifah ranges between ~520–550 °C and 18–22 kbar (El-Shazly et al., 1990, 1994, 1997, 2001; Miller et al., 1998, 2002; Warren and Waters, 2006; Yamato et al., 2007; Massonne et al., 2013). Fig. 1 shows the regional geology around of As Sifah region consists of Mesozoic–Tertiary rock units occurred southeast of Muscat, Oman.

The multi-spectral remote sensing technique is widely utilized, particularly to the regions that have extremely rugged topography, where it is impossible to do exhaustive sampling and detailed conventional geological mapping. Several studies show the potential of multi-spectral remote sensing technique to map different lithological units and structures in arid region and considered the tool as a cost-effective alternative to an expensive and time-consuming field mapping technique (Sultan and Arvidson, 1986; Abrams et al., 1988; Abrams and Hook, 1995; Abdelsalam et al., 2000; Bedell, 2001; Ferrier et al., 2002; Kusky and Ramadan, 2002; Gad and Kusky, 2006; Liu et al., 2007; Khan and Mahmood, 2008; Amer et al., 2010; Rajendran et al., 2011a, 2012, 2014). Since 2000, the multispectral ASTER satellite data have been extensively and successfully used in mapping of lithologies and structures, and exploration of mineral and ore deposits (Crósta and Filho (2003), Rowan et al. (2005), Ninomiya et al. (2005, 2006), Gad and Kusky (2007), Zhang et al. (2007), Rockwell and Hofstra (2008), Gabr et al. (2010), Rajendran et al. (2012, 2013), Rajendran and Nasir (2013a,b, 2014a,b,c)). However, very little attention is paid to discriminate metamorphic zones in these areas. Study on the use of low-cost multispectral satellite data and simple well known image-processing methods to map metamorphic zones and discriminate metamorphic rocks are of great importance and helpful to the geologists working in tectonism and associated metamorphism. Therefore, the main objective of this study is to map the region of high pressure metamorphic zone and discriminate their metamorphic rocks by studying spectral characters of metamorphic minerals in VNIR–SWIR spectral regions using the remotely sensed low-cost ASTER satellite data and well known image processing methods. This study demonstrates the mapping of metamorphic zone of As Sifah region of southeast of Muscat, Oman (Fig. 1).

2. Geology of As Sifah area

Regional geological mapping across northern Saih Hatat window of NE Oman has been carried out by Le Métour et al. (1986) and Miller et al. (2002). The region exposes metamorphosed basement and continental shelf rock units structurally overlain by the Samail ophiolite and the Hawasina complex. In this study, we focus the area around As Sifah dome which is the deepest exposed part of the Oman Mountains and plunges north towards Muscat and south towards Quriat. Here, the garnet + clinopyroxene + glaucophane + phengite + epidote eclogites were developed at pressure around 20 kbar and formed the core of the dome (Goffé et al., 1988; El-Shazly, 1994; Searle et al., 1994, 2004). They are surrounded by highly deformed calc-schists and quartz mica schists mapped as metamorphosed Saiq Formations of Late Permian age. The meta-basic eclogites on the beach north of As Sifah are metamorphosed Saiq volcanics. The blueschist-eclogite facies of As-Sifah that crops out along the eastern coast have been affected by high P–T metamorphic events (El-Shazly and Lanphere, 1992) and petrological studies on these rocks are carried out extensively by Goffé et al. (1988), El-Shazly et al. (1990, 1997), Le Métour et al. (1990), Wendt et al. (1993), Searle et al. (1994), Miller et al. (1998, 2002) and Warren et al. (2003).

The study region (Fig. 2) shows no significant tonal variation on the False Colour Composite (FCC) ASTER image (Fig. 2a; R:3, G2, B1) and is occurred with predominantly two major group of rock formations viz. the autochthonous units and the Quaternary formations (Fig. 2b). The autochthonous units consist of the high pressure metamorphic rocks namely calcareous schist with black limestone (Sq1Cs), schists with white tuff (Sq1V) intruded with dolerite sills and dykes (SqDI) and eclogites. The rocks are associated with the carbonate rocks consist nodular limestone, yellow dolomite, silicified limestone (region of Sq1L), and black colored fusilinid limestone and dolomite (Sq2a). These are over lined by alluvial fans and terraces, and active slope and scree deposits of Quaternary formations of Sub-recent age. The recent deposits such as coastal dunes and beach sands are occurred parallel to the coast line in the study region (Fig. 2b).

Please cite this article in press as: Rajendran, S., Nasir, S. Mapping of high pressure metamorphics in the As Sifah region, NE Oman using ASTER data. Adv. Space Res. (2014), http://dx.doi.org/10.1016/j.asr.2014.11.026

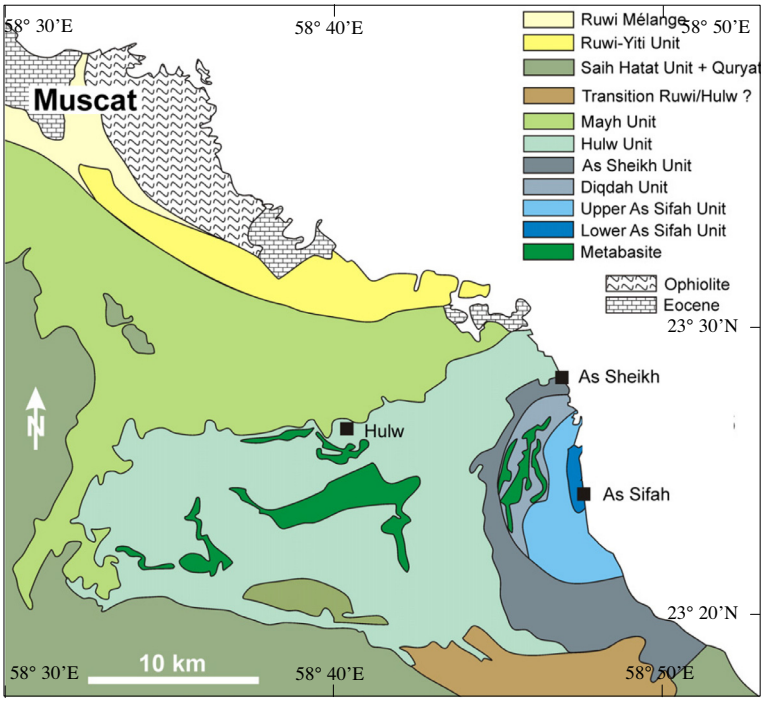

Fig. 1. Geological map showing the Mesozoic–Tertiary rock units, southeast of Muscat, Oman. (Source: Massonne et al. (2013); this map was simplified on the basis of a map presented by Yamato et al. (2007)).

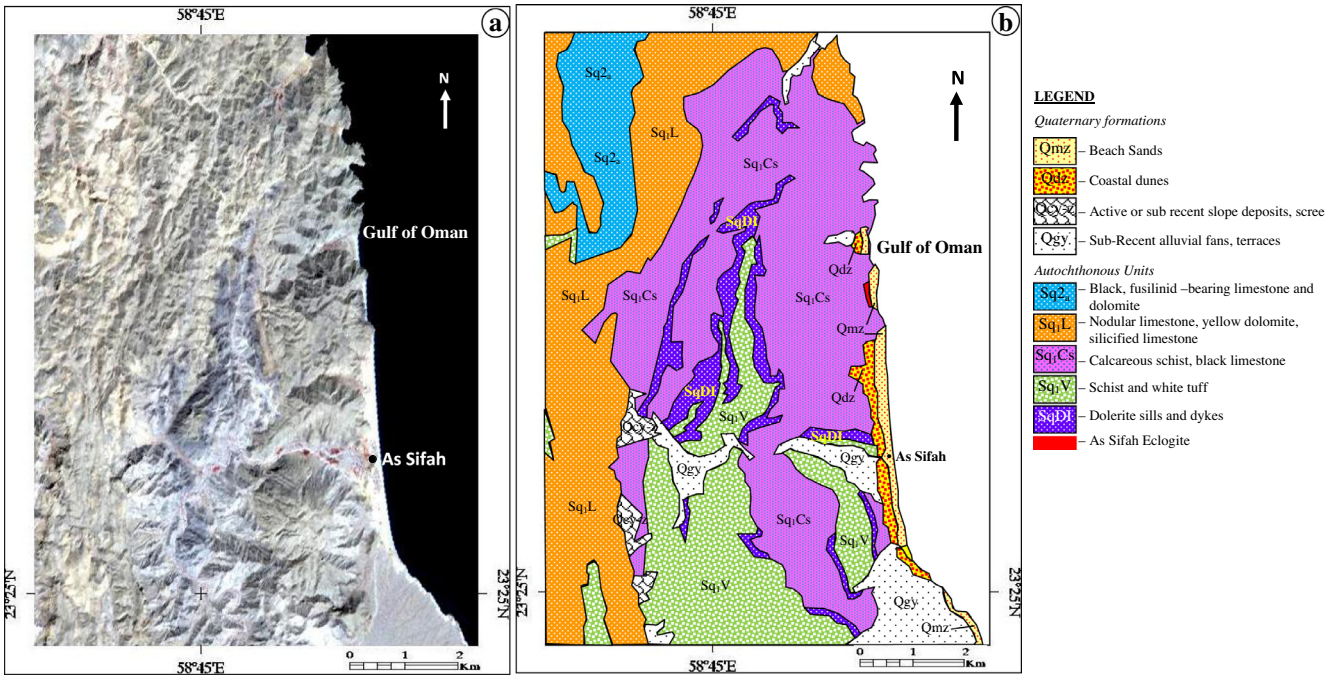

Fig. 2. (a) ASTER RGB (R:3, G:2; B:1) image and (b) geology around of As Sifah region (modified from Ministry of Petroleum and Minerals, 1986).

3. Spectral characters of metamorphic minerals

Metamorphic minerals show significant spectral absorption characters for remote identification. The reflectance spectrum of metamorphic rock depends on the minerals composition of the rock surface, which is usually a mixture of the whole rock mineralogy and weathering of minerals. Several studies on spectral measurement of minerals and rocks are carried out and cited in geological remote sensing (Hunt et al., 1973, 1974; Adams, 1974; Hunt and Ashley, 1979; Clark et al., 1990) to understand their spectral absorption characters. Since the absorption features are

Please cite this article in press as: Rajendran, S., Nasir, S. Mapping of high pressure metamorphics in the As Sifah region, NE Oman using ASTER data. Adv. Space Res. (2014), http://dx.doi.org/10.1016/j.asr.2014.11.026

specific to each mineral, it is possible to detect the different minerals and to estimate their relative proportions in the rocks (Combe et al., 2006; Clènet et al., 2010). Comprehensive spectral absorption-compositional studies can provide important insight to the causes of spectral variation and quantitative data for use in the interpretation of optical remote sensing data (Rowan and Mars, 2003; Ninomiya et al., 2005; Corrie et al., 2010; Mars and Rowan, 2010; Rajendran et al., 2012; Rajendran and Nasir, 2013a). Hunt and Salisbury (1970), Hunt et al. (1973, 1974), Hunt and Ashley (1979) and Blom et al. (1980) showed the spectra of metamorphic minerals and provided their significant spectral absorption characters in the spectrum of visible and near infrared regions. The spectra of selected metamorphic minerals with other minerals stacked from the USGS Spectral Library for minerals (Envi 5) is given in Fig. 3. The minerals such as augite ((Ca, Na)(Mg, Fe^{2+}, Al Fe^{3+}, Ti)(Si, Al)$_2O_6$), diopside ($CaMgS_2O_6$), hornblende (Ca_2(Mg, Fe, Al)$_5$(Al, Si)$_8O_{22}(OH)_2$), actionalite (Ca_2(Mg, Fe)$_5Si_8O_{22}(OH)_2$), biotite (K(Fe, Mg)$_3AlSi_3O_{10}$(OH, F)$_2$), pyrope ($Mg_3Al_2Si_3O_{12}$), epidote (Ca_2(Al, Fe)$_3(SiO_4)_3(OH)$), glaucophane (Na_2(Mg, Fe)$_3Al_2Si_8O_{22}(OH)_2$), chlorite ((Mg, Fe^{2+})$_5$Al(Si_3A)$O_{10}(OH)_8$), pyrophyllite ($Al_2(OH)_2/Si_4O_{10}$), paragonite ($NaAl_2(Si_3Al)O_{10}(OH)_2$), illite ($K_{0.65}Al_{2.0}(Al_{0.65}Si_{3.35}O_{10})(OH)_2$), albite ($4NaAlSi_3O_8$), calcite ($CaCO_3$), dolomite (CaMg $(CO_3)_2$),

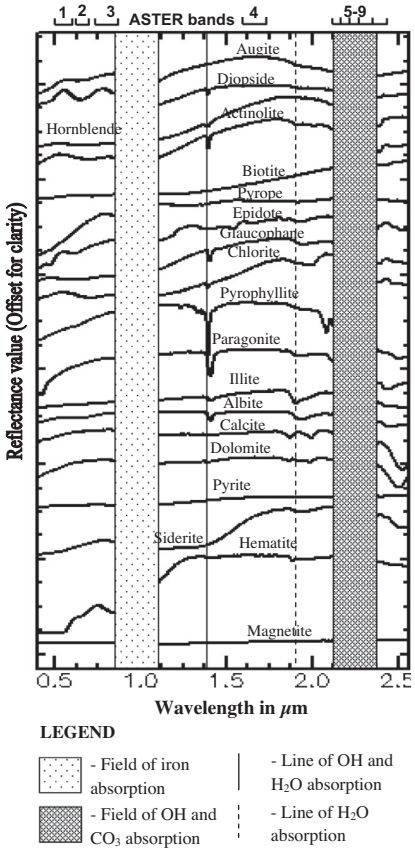

Fig. 3. Spectra of major minerals of metamorphic rocks stacked from the USGS Spectral Library for minerals.

pyrite (FeS_2), siderite ($FeCO_3$|), hematite (Fe_2O_3) and magnetite (Fe_3O_4) show significant useful narrow absorption features near 0.5 μm and in between 0.9 and 1.1 μm due to iron absorption (the field dotted in Fig. 3), near 1.4 μm due to OH and H_2O absorptions (the vertical line in Fig. 3), near 1.9 μm mainly due to H_2O absorption (the vertical dashed line in Fig. 3), and around 2.2–2.3 μm due to OH and CO_3 absorptions (the field dark dotted in Fig. 3) which are closer to the ASTER sensor spectral wavelengths 0.52–0.60 μm (likely to band 1), 0.76–0.86 μm (likely to band 3), 1.6–1.7 μm (band 4), 2.145–2.185 μm (band 5), 2.185–2.225 μm (band 6), and 2.295–2.365 μm (band 8).

In the plot (Fig. 3), the spectra of hematite, siderite, epidote, actinolite, hornblende, augite and diopside minerals show absorptions around 0.5 and 1 μm due to the iron (Fe^{2+}, Fe^{3+}) content present in their lattices (Abrams et al., 1988; Rajendran et al., 2011b, 2013, 2014; Rajendran and Nasir, 2014c). The spectra of the carbonate minerals namely dolomite, calcite and siderite have significant absorptions near 2.3 μm due to C–O bonds in their compositions (Hunt, 1977; Abrams et al., 1988; Mars and Rowan, 2010; Rajendran et al., 2012, 2013, 2014; Rajendran and Nasir, 2014a,b). The significant spectral absorptions around 1.4, 1.9, 2.2 and 2.3 μm in clays, micas, and amphiboles minerals are due to presence of hydroxyl contents in their contents. The hydroxyl and H_2O-bearing minerals show absorptions at 1.4 and near 1.9 μm (H–O–H bendings and OH stretches, Hunt et al., 1974; Abrams et al., 1988; Rajendran et al., 2012, 2014). Al–OH produces absorption centered at about 2.2 μm, whereas Mg–OH produces feature at about 2.3 μm spectral wavelengths (Hunt, 1977, 1979; Abrams et al., 1988; Mars and rowan, 2010; Rajendran et al., 2012, 2014; Rajendran and Nasir, 2014c). The light absorptions stretched near 1.7 and 2.1 μm in the illite, paragonite, pyrophyllite, glaucophane and chlorite may be due to the influence of Fe, Mg, Ca, Na and Al contents in the minerals. Based on the spectral absorption characters of such minerals, the minerals bearing rock types can be discriminated over satellite data using several image processing methods including false color composites, band ratios, decorrelation stretching, and principal components analysis (Sultan et al., 1987; Ninomiya, 2002; Ninomiya et al., 2005; Corrie et al., 2010; Rajendran et al., 2011a,b, 2012, 2013, 2014; Rajendran and Nasir, 2013a,b, 2014a,b,c). The study region is dominantly occurred with varieties of metamorphic schists and carbonate rocks (Fig. 2b) composed with the discussed minerals. Thus, the occurrence of metamorphic zone and rock types of As Sifah region can be delineated and discriminated using the ASTER spectral bands 1, 3, 4, 5, 6 and 8 in the VNIR–SWIR regions.

4. Satellite data and methods

ASTER sensor is a multispectral imaging system, launched during December 1999 travels in a near circular,

Please cite this article in press as: Rajendran, S., Nasir, S. Mapping of high pressure metamorphics in the As Sifah region, NE Oman using ASTER data. Adv. Space Res. (2014), http://dx.doi.org/10.1016/j.asr.2014.11.026

Table 1
Sensor characteristics of ASTER instruments.

Sensors	ASTER		
Characteristics	VNIR	SWIR	TIR
Spectral bands	Band 01 0.52–0.60 Nadir looking	Band 04 1.6–1.7	Band 10 8.125–8.475
With range (μm)	Band 02 0.63–0.69 Nadir looking	Band 05 2.145–2.185	Band 11 8.475–8.825
	Band 03 N 0.76–0.86 Nadir looking	Band 06 2.185–2.225	Band 12 8.925–9.275
	Band 03B 0.76–0.86 Backward looking	Band 07 2.235–2.285	Band 13 10.25–10.95
		Band 08 2.295–2.365	Band 14 10.95–11.65
		Band 09 2.36–2.43	
Spatial Resolution (m)	15	30	90
Swath width (km)	60	60	60
Radiometric Resolution (bits)	8	8	8
Cross track Pointing	±318 km (±24 deg)	±116 km (±8.55 deg)	±116 km (±8.55 deg)

sun-synchronous orbit with an inclination of approximately 98.28, an altitude of 705 km and a repeat cycle of 16 days. The sensor measures visible reflected radiation in three spectral bands, infrared reflected radiation in six spectral bands and emitted radiation in five spectral bands. The sensor characteristics of ASTER are provided in Table 1 and can be referred more in Fujisada (1995), Rajendran et al. (2011a, 2012), Rajendran and Nasir (2013a) and http://asterweb.jpl.nasa.gov/content/03_data/04_Documents/aster_user_guide_v2.pdf. In the present study, the ASTER level 1B scene (AST_L1B_00305092004064558_20140106130013_2217), acquired on May 09, 2004, obtained from NASA Land Processes Distributed Active Archive Center User Services, USGS Earth Resources Observation and Science (EROS) Center (https://LPDAAC.usgs.gov) is used. The data were delivered in a Tag Image File (.TIF) format consists of imagery and an ASCII text (.met) file of metadata. The imagery were checked and found in the cloud cover of 0% and for sensor errors, such as banding and other geometric distortions. The data were supplied in terms of scaled radiance at sensor data with radiometric and geometric corrections applied. The data were georeferenced in the UTM projection and for the WGS-84 ellipsoid. Among 14 spectral bands, nine VNIR–SWIR spectral bands were resampled to 15 mts. and chosen to process the region of interest to map the metamorphic rocks of the As Sifah region using ENVI (5) and ArcGIS (10) softwares. Delineation of metamorphic zone from the carbonate rocks, discrimination of metamorphic rock types and detecting of minerals of the rocks are carried out by decorrelation stretch, PCA and SAM image processing methods. The occurrence and spatial distribution of major lithological units are assed for accuracy by confusion matrix using Maximum Likelihood (ML), Spectral Angle Mapper (SAM) and Spectral Information Divergence (SID) algorithms. Interpreted images are verified in the field using geological map (Ministry of Petroleum and Minerals, 1986) available in the scale 1: 100,000. Samples collected from the field were analyzed at Department of Earth Sciences and Central Analytical and Applied Research Unit (CAARU) of Sultan Qaboos University to identify and confirm the minerals of the formations. The details of the studies are given in Table. 2.

5. Image analysis

Ophiolite sequence of Sultanate of Oman consist a wide range of lithologies and associated features such as metamorphism, alteration, weathering and vegetation which play a role in mixing and muting spectral signals of different lithologies. Many authors have used different image processing methods such as band ratioing, decorrelation stretching, Principal Component Analysis and Spectral Angle Mapper (supervised classification method) to discriminate different lithology, structures, alteration zones and detecting of minerals etc. on different satellite images including Landsat TM and ETM, ASTER and hyperspectral sensors (Crosta et al., 1998; Abdelsalam et al., 2000; Ferrier et al., 2002; Ninomiya, 2002; Galvao et al., 2005; Rowan et al., 2005; Rown et al., 2006; Tangestani et al., 2008; Khan and Mahmood, 2008; Amer et al., 2010; Clénet et al., 2010; Gabr et al., 2010; Tangestani et al., 2011; Rajendran et al., 2013; Rajendran and Nasir, 2014c). The lithologies of arid region are mapped by well known image processing methods such as decorrelation stretch (Gillespie et al., 1986; Rothery, 1987; Abrams et al., 1988; Matthews and Jones, 1992; Philip et al., 2003; Rajendran et al., 2012; Rajendran and Nasir, 2014a), PCA (Azizi et al., 2007; Khan et al., 2007; Amer et al., 2010; Gabr et al., 2010; Rajendran et al., 2011a,b, 2013a; Rajendran and Nasir, 2013a), minimum noise fraction (Green et al., 1988) and Spectral Angle Mapper

Please cite this article in press as: Rajendran, S., Nasir, S. Mapping of high pressure metamorphics in the As Sifah region, NE Oman using ASTER data. Adv. Space Res. (2014), http://dx.doi.org/10.1016/j.asr.2014.11.026

Table 2
Details on the field samples study.

Study	Number of samples studied/taken spectral measurements	Equipments/instruments used	Purpose of study	Laboratory
Microscope study	42	Microscope (OPTIKA, B600POL-1)	Study of minerals property	Department of earth sciences
Spectral measurements	350	PIMA SP infrared spectrometer with PIMA VIEW software	Absorption characters of minerals	
X-ray powder diffraction (XRD) study	27	X'Pert PRO	Occurrence of minerals and to confirm the microscopic and spectral studies	Central analytical and applied research unit (CAARU)

(Rowan et al., 2005; Khan and Glenn, 2006; Khan et al., 2007; Hecker et al., 2008; Gabr et al., 2010; Rajendran et al., 2013; Rajendran and Nasir, 2014a,b,c). Rowan and Mars (2003) studied the ASTER spectral reflectance data and provided a basis for mapping of limestone and dolomite exposures, distinguishing Al-muscovite from Fe-muscovite, delineating rocks containing Fe, Mg–O–H minerals, such as chlorite, hornblende, epidote and biotite, and Al–O–H minerals and skarn deposits with associated marble. They showed the ASTER Relative Band-Depth (RBD) image of band ratio, (band 5 + band 7)/band 6, to the occurrence of Al–O–H rich muscovite minerals. Gad and Kusky (2007) studied the ASTER band-ratio (4/7-4/6-4/10) image for lithological mapping of Arabian–Nubian shield, the Neoproterozoic Wadi Kid area, Sinai, Egypt, and discriminated the major rock types namely gneiss and migmatite, amphibolite, volcanogenic sediments with banded iron formation, meta-pelites, talc schist, meta-psammites, meta-acidic volcanics, meta-pyroclastics volcaniclastics, albitites and granitic rocks. Azizi et al. (2007) used SWIR bands of ASTER and interpreted the image for presence of hydrothermal altered minerals in propylitic and phyllic alteration zone to the exploration of copper and gold mineralization occurred to the SE of Sanandaj city situated in Kurdistan Province, west of Iran. They studied the images of band ratios and PCA, and described the propylitic zone rich in chlorite and epidote minerals, and phyllic zone rich in white mica and kaolinite minerals.

In the present study, we used the decorrelation stretching and PCA image processing methods to delineate the metamorphic zone and discriminate the metamorphic rock types of the study region. Decorrelation stretching method is widely used and discussed by Gillespie et al. (1986), Rothery (1987), Abrams et al. (1988), Matthews and Jones (1992), Philip et al. (2003) and Rajendran and Nasir (2013a, b). It is based on a principal component transformation of the acquired data. Here, the transformed channels are contrast stretched and arbitrarily assigned primary colors for display as a color composite image. Abrams et al. (1988) mapped the Oman ophiolite using enhanced Landsat Thematic Mapper data by decorrelation stretching method and showed the capacity of data and method to distinct the spectral reflectance of different rock types and their weathering products. Further, they stated that the method produces image (RGB: 7, 5 and 4) capable to recognize variations in gabbro composition and to identify small acidic, gabbroic and ultramafic intrusions. The method is being used by Rajendran et al. (2012) for discrimination of the ophiolite sequences of Samail ophiolite of Sultanate of Oman. During 2014, Rajendran and Nasir (2014a) studied the method and discriminated the limestone formations and associated lithology occurred at Tanuf valley and near Sur region of parts of Sultanate of Oman using ASTER spectral bands 8, 3, and 1. To map the metamorphic zone of the As Sifah region, the advantage of the visible and short wavelength infrared reflectance properties of minerals of the metamorphic rocks are studied over ASTER spectral bands as discussed in Section 3. Based on, the ASTER spectral bands 5, 6 and 8 were processed using this method and the resulted RGB image is given in Fig. 4 for further discussion.

Further, to discriminate the metamorphic rocks and carbonate formations of As Sifah region, the application of PCA method is used. In this technique, the relationship between the spectral response of target minerals or rocks and numeric values extracted from the eigenvector matrix is used to calculate the principal component (PC) images. Using this relationship, one can determine which PC contains the information due to minerals and rocks, and whether the digital numbers (DNs) of pixels containing the target minerals and rocks had high (bright) or low (dark) values (Crósta and Moore, 1989; Loughlin, 1991; Rokos et al., 2000; Crósta and Filho, 2003; Rajendran et al., 2011a, 2012). Since, the study region consists of hydroxyl bearing aluminosilicates (have significant absorptions in ASTER bands 4, 5 and 6) and carbonate minerals (have absorptions in ASTER band 8) bearing rocks, the ASTER SWIR bands were chosen for a PCA analysis (e.g. Richards and Xiuping (1998)) to discriminate the rocks of the study region. The pre-treatment and processing of ASTER spectral bands for above said technique are followed as stated in Abdeen et al. (2001) and Amer et al. (2010). It is generally accepted that the first three high order principal components (1, 2, and 3) of PCA have over 99% of the spectral information; hence these have been widely used for lithological mapping rather than

Please cite this article in press as: Rajendran, S., Nasir, S. Mapping of high pressure metamorphics in the As Sifah region, NE Oman using ASTER data. Adv. Space Res. (2014), http://dx.doi.org/10.1016/j.asr.2014.11.026

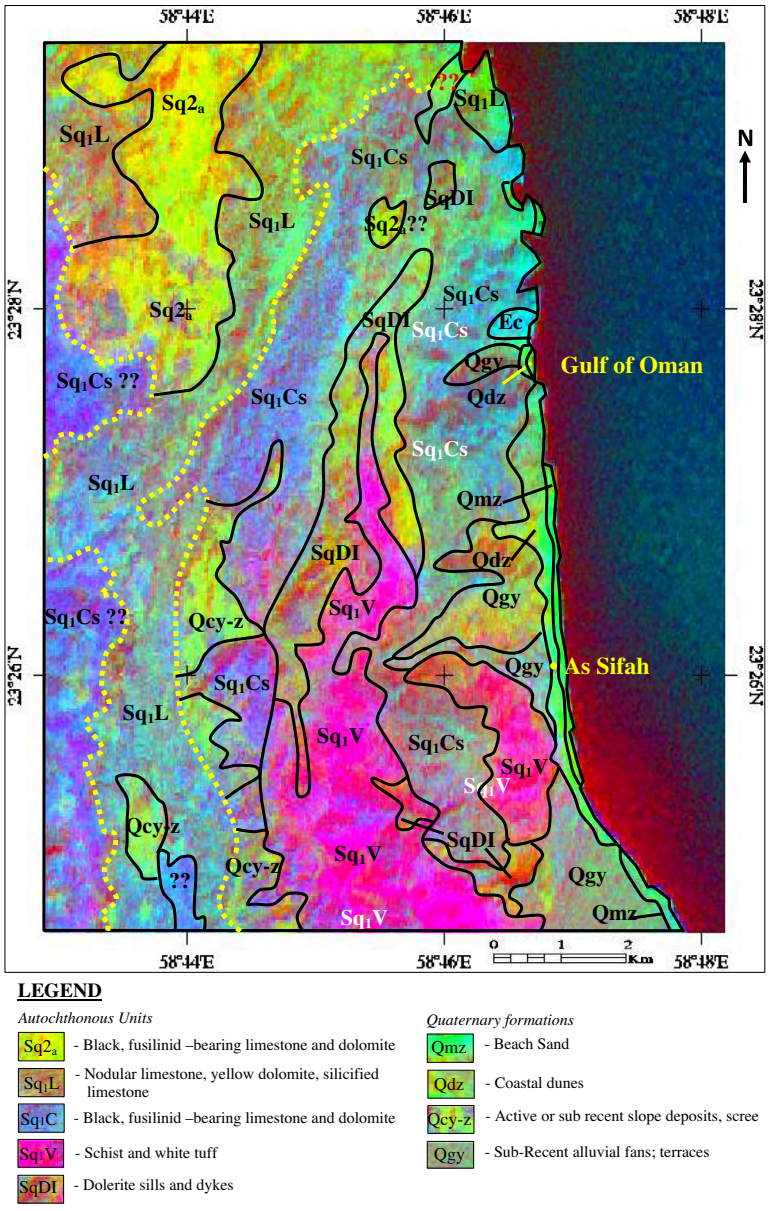

Fig. 4. Decorrelated image of ASTER spectral bands 5, 6 and 8 shows the high pressure metamorphic zone in the As Sifah region.

the subsequent low order principal components (4 and 5) which usually contains less than 1% of spectral information and low signal-to-noise ratios. However, some of the higher order principal components provide subtle information about the occurrence of minerals and rock types that are spatially dominant in the image. The study of bright reflections and dark absorptions of individual component of PCA of the study region (Rajendran et al., 2011a, 2012) allowed choosing the principal components of PC4, PC3 and PC2 (Fig. 5) to discriminate the metamorphic rocks of As Sifah region. The RGB image developed using the principal components (R:PC4, G:PC3, B:PC2) is given in Fig. 6 for discussion in the following section.

Apart to the delineation of metamorphic zone and the discrimination of metamorphic rocks of the study region using the decorrelation stretching and PCA image processing methods, an attempt is also made to extract informations on the occurrence of metamorphic minerals to confirm the presence of the rock types of the study region using supervised classification method called Spectral Angle Mapper (SAM). The SAM was found useful in mapping the lithologies and minerals (Rowan et al., 2003; Khan and Glenn, 2006; Khan et al., 2007; Hecker et al., 2008; Rajendran et al., 2013; Rajendran and Nasir, 2014c). The method encompasses the hyperspectral tools such as Minimum Noise Fraction (MNF) transformation, Pixel Purity Index (PPI) and *n*-Dimensional visualize, and classifying minerals based on collection of end-member spectral informations (Kruse et al., 2003; Gabr et al., 2010; Rajendran et al., 2013; Rajendran and Nasir, 2014c).

Please cite this article in press as: Rajendran, S., Nasir, S. Mapping of high pressure metamorphics in the As Sifah region, NE Oman using ASTER data. Adv. Space Res. (2014), http://dx.doi.org/10.1016/j.asr.2014.11.026

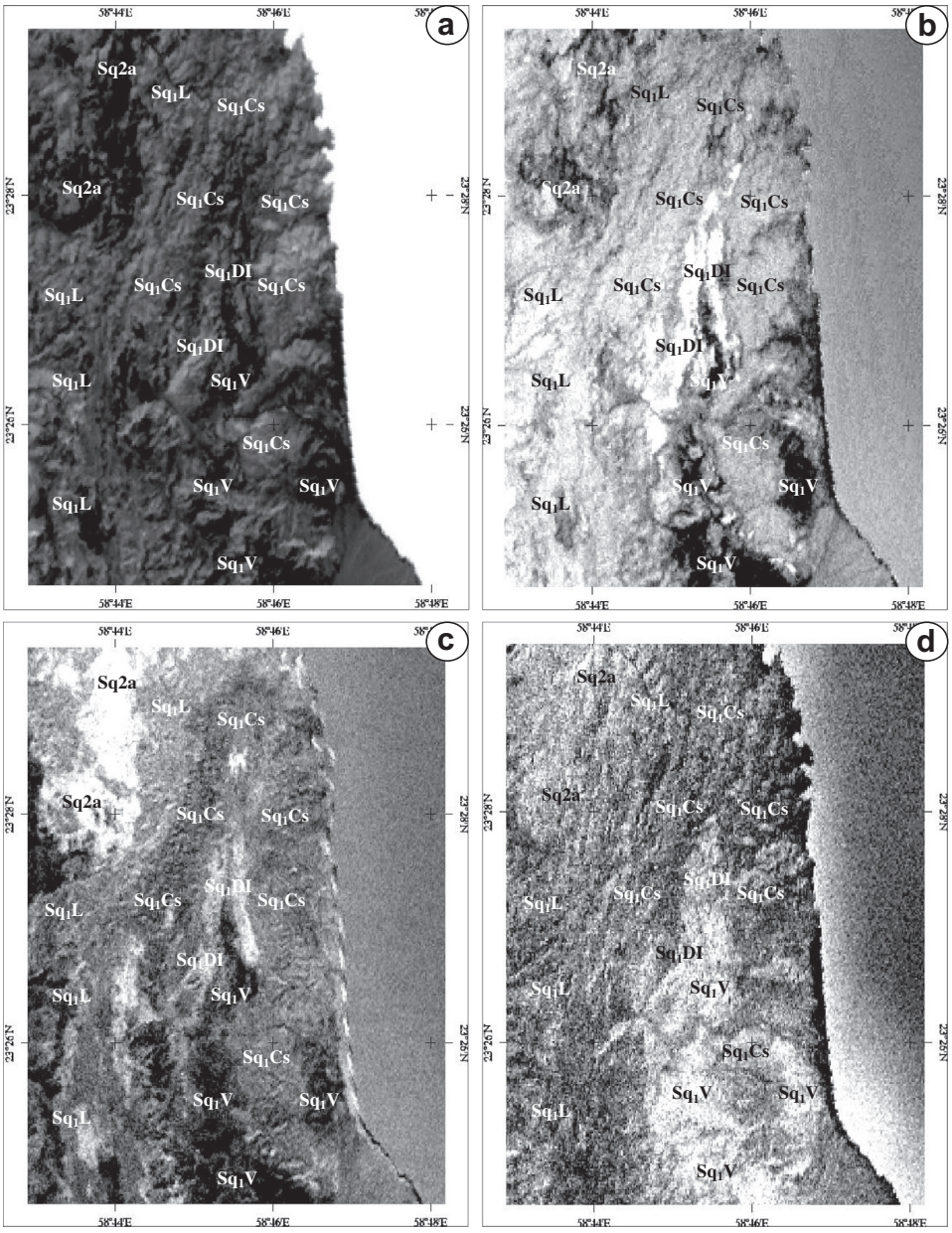

Fig. 5. (a–d) Image of principal components (PC1–PC4) of ASTER SWIR spectral bands of the study region shows the occurrence of major rock formations consist of hydroxyl bearing silicates and carbonates (Schist and white tuff (Sq1V); calcareous schist with black limestone (Sq1Cs); dolerite sills and dykes (SqDI); nodular limestone, yellow dolomite, silicified limestone (Sq1L); black colored fusilinid limestone and dolomite (Sq2a)).

6. Results and discussion

6.1. Delineation of As Sifah metamorphic zone

The decorrelated RGB image developed using the ASTER spectral bands 5, 6 and 8 is given in Fig. 4. Here, the ASTER band 8 is chosen to show the occurrence of carbonate minerals bearing rocks (the band also stretches the OH molecules bearing minerals, Abrams et al., 1988; Rajendran et al., 2012, 2013), the band 6 is selected to provide information related to Al–OH minerals bearing rocks (Rowan and Mars, 2003; Gad and Kusky, 2007) and the band 5 is chosen to highlight the Ca, Na and Al contents rich minerals bearing rocks to delineate the metamorphic zone from carbonate formations in the study region. The image shows the occurrence and distribution of region of metamorphic zone which consists predominantly the variety of schist and eclogite rocks, and delineated (interpreted by dotted lines) from the carbonate rocks in the study region. In the image, the eclogite, schist and white tuff, and calcareous schist with black limestone are appeared in dark pink to mixture of pale blue colors. The dolerite sills and dykes intrusions are shown in the shades of red and yellow colors. The carbonate formation consist nodular limestone, yellow dolomite, silicified limestone, and black colored fusilinid limestone and dolomite are

Please cite this article in press as: Rajendran, S., Nasir, S. Mapping of high pressure metamorphics in the As Sifah region, NE Oman using ASTER data. Adv. Space Res. (2014), http://dx.doi.org/10.1016/j.asr.2014.11.026

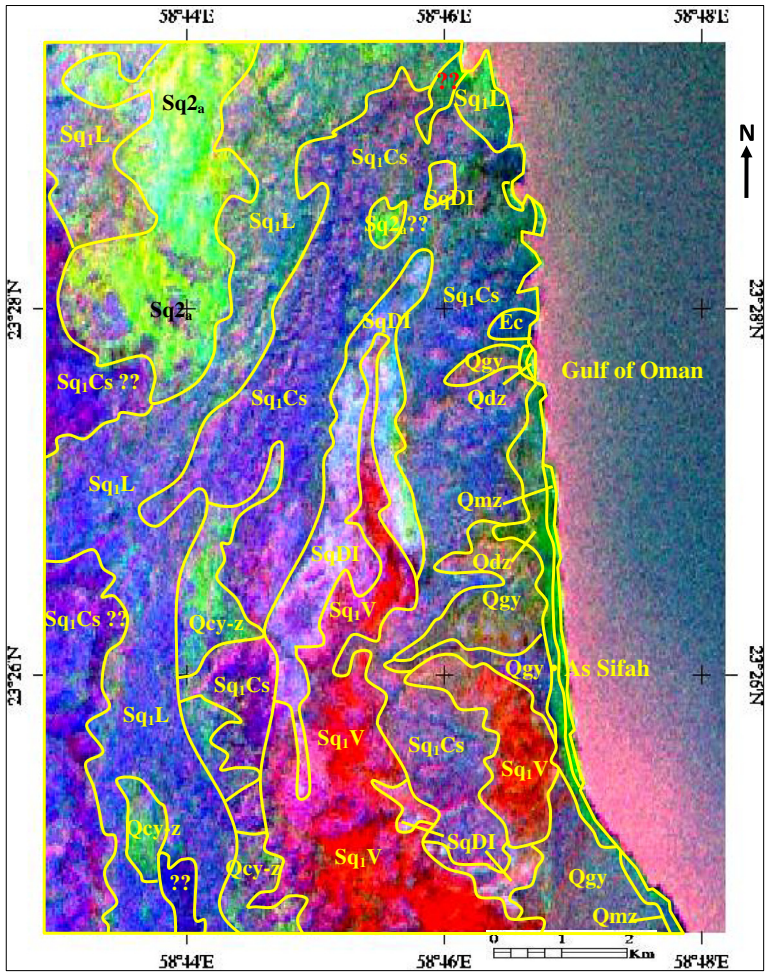

LEGEND

Autochthonous Units

- $Sq2_a$ - Black, fusilinid –bearing limestone and dolomite
- Sq_1L - Nodular limestone, yellow dolomite, silicified limestone
- Sq_1C - Black, fusilinid –bearing limestone and dolomite
- Sq_1V - Schist and white tuff
- SqDI - Dolerite sills and dykes

Quaternary formations

- Qdz/Qmz - Coastal dunes (green)/ Beach Sand (yellow)
- Qcy-z - Active or sub recent slope deposits, scree
- Qgy - Sub-Recent alluvial fans; terraces

Fig. 6. The ASTER RGB image of principal components PC4, PC3 and PC2 shows the occurrence and spatial distribution of hydroxyl bearing metamorphic rocks and carbonate formations in the As Sifah region.

appeared in dark blue to bright yellow in colors. The occurrence of eclogite exposures near coastal region is interpreted in shade of blue–cyan colors. The Quaternary formations are appeared in the shades of light green to pale blue colors. The interpreted image is correlatable with the geological map (Fig. 2b). The ASTER spectral bands (5, 6, and 8) processed using decorrelation stretching method are proved beneficial in the delineation of metamorphic zone of the study area.

6.2. Discrimination of metamorphic rock units

In the PCA analysis, the six SWIR bands were used for the calculation of eigenvector and eigenvalue (Table 3) to discriminate the major rock types of the study area. The calculated eigenvector matrixes are used to identify the PC contain the hydroxyl bearing metamorphic minerals for discrimination of metamorphic rocks and the PC contains the informations on carbonates formations of the study area. Among the six ASTER SWIR bands processed by PCA, the components PC5 and PC6 are not provided any significant informations and exhibit with more noise. Thus, the images of first four principal components are given in Fig. 5a–d for discussion. The eigenvalue (Table 3) shows about 99.81% to band 4, 0.13% to band 5, 0.027% to band 6 and 0.014 to band 7, and 0% to the bands 8 and 9. In the Table 3, the eigenvector values of PC1 show the negative values in all bands. The PC2 shows negative value in band 4 and positive value in bands 5, 6 and 7. The PC3 shows the bright reflection in band 7 and the absorption

Please cite this article in press as: Rajendran, S., Nasir, S. Mapping of high pressure metamorphics in the As Sifah region, NE Oman using ASTER data. Adv. Space Res. (2014), http://dx.doi.org/10.1016/j.asr.2014.11.026

Table 3
The matrix of eigenvector for 6 SWIR bands.

Eigenvector	Band 4	Band 5	Band 6	Band 7	Band 8	Band 9
PC1	−0.905195	−0.242513	−0.234647	−0.208404	−0.134143	−0.072961
PC2	−0.419335	0.443671	0.503065	0.433468	0.311747	0.298595
PC3	−0.003540	0.218855	0.586391	−0.651608	−0.422887	0.069350
PC4	−0.029050	0.817823	−0.538324	−0.099573	−0.173390	−0.023439
PC5	−0.061688	0.125819	0.240883	0.284526	−0.186063	−0.898201
PC6	−0.010878	0.108538	0.013925	−0.503201	0.800814	−0.305604
Eigen value in %	99.81	0.13	0.027	0.014	0.00	0.00

in bands 5 and 6. The PC4 shows the maximum negative value in band 6 and positive value in band 5. The image of PC1 (Fig. 5a) shows the Gulf of Oman in very bright reflection and the lithological units of surface are not showing any significant differences in dark absorption. The image of PC2 (Fig. 5b) highlights the intrusives by bright reflection, and the occurrence of schist and white tuff and black colored fusilinid limestone and dolomite by strong absorption. Therefore, the PC2 is chosen to discriminate the rock types from the occurrence of the intrusives. The image of PC3 (Fig. 5c) shows the occurrence of black colored fusilinid limestone and dolomite by bright reflection, and the schist and white tuff and calcareous schist with black limestone by dark absorptions. The formation consists of nodular limestone, yellow dolomite, and silicified limestone is appeared in grey tone and distinguishable from other rock types. Thus, the PC3 is chosen to show variations among the rock types. The chosen PC3 increases the information on the occurrence of schist and white tuff with PC2. The PC4 image (Fig. 5d) shows the schist and white tuff in bright reflection and other rock types including nodular limestone, yellow dolomite, and silicified limestone in the grey scale color. The component is chosen to distinguish the occurrence of schist and white tuff from the other rock units. The poorly correlated noisy principal components such as PC5 and PC6 showed very poor in eigenvector values in the bands 4, 5, 6, and 7 are not considered for discrimination of rocks of the region.

Since the principal component bands PC2, PC3 and PC4 show significant informations on the occurrence of different rock types, a RGB image is developed using the three PC bands (R:PC4, G:PC3, B:PC2; Fig. 6) for better discrimination and mapping of different rock types, and distinguish the OH bearing metamorphic rocks from the carbonate formations in the study region. The image shows all formations of the area in different tone and easily distinguishable. The black colored fusilinid limestone and dolomite show its occurrence in mixture of pale yellow and green colors. The formation consists of nodular limestone, yellow dolomite and silicified limestone are appeared in pale purple color with fine texture occurred in between the black colored fusilinid limestone and dolomite, and calcareous schist with black limestone formations. The formation consists of calcareous schist with black limestone is appeared in pink to purple colors and coarse texture. The schist and white tuff exhibits dark pink to red colors due to strong absorption. The absorption may be due to the presence of OH bearing metamorphic minerals in the rocks. The dolerite sills and dykes (poorly altered compared to other rocks) are appeared in pale bluish white colors due to the poor absorption and high reflection. The variation in absorptions may be due to presence of the iron–magnesium rich pyroxene minerals and absence of hydroxyl minerals. In the Quaternary formations, the beach sand and coastal dunes are appeared in dark green color, and the active or sub recent slope deposits, scree, alluvial fans and terraces are exhibited with the mixture of red–yellow–green colors. The formation consists of nodular limestone, yellow dolomite, and silicified limestone showed in geological map (Fig. 2b) occurred at south west and west regions in the image show variation in colors (pink to purple colors with coarse texture marked by ?) which requires a detailed geological study. The metamorphic rocks such as the calcareous schist with black limestone (pink to purple colors) and schist and white tuff (dark pink to red colors) are well discriminated within the region of metamorphic zone as delineated in the decorrelated image (Fig. 4) from the other carbonate rich formations. The study shows that the PCA image (Fig. 6) is powerful in the discrimination of metamorphic rocks and distinguishes them from the carbonate formations of the study area.

6.3. Accuracy assessment

Study of accuracy for the occurrence and spatial distribution of the metamorphic rocks and associated carbonate formations are important to assess the capability of used techniques. In this study, accuracy assessments by confusion matrix are carried out to differentiate image classification algorithms namely Maximum Likelihood (ML), Spectral Angle Mapper (SAM) and Spectral Information Divergence (SID) (Chen and Reed, 1987; Congalton, 1991; Sabol et al., 1992; Jia and Richards, 1994; Van Der Meer, 1995; Zhang et al., 2007; Bedini, 2011; Hosseinjani and Tangestani, 2011; El Janati et al., 2014). The confusion matrix provides the accuracy of a classification result by comparing a classification result with ground truth information. The ground truth can be provided as ground truth image or ground truth ROIs. The procedure computes overall accuracy, producer and user accuracies, Kappa Coefficient, and errors of commission and omission (Envi 5). Since the library and field spectra were not acquired

Please cite this article in press as: Rajendran, S., Nasir, S. Mapping of high pressure metamorphics in the As Sifah region, NE Oman using ASTER data. Adv. Space Res. (2014), http://dx.doi.org/10.1016/j.asr.2014.11.026

under the same conditions of satellite image and the image endmembers are directly associated with surface components detectable in the scene, we studied the spectral absorption characters of the endmembers extracted from the image by PPI algorithms and image spectra, and used ground truth ROI's for accuracy assessment in this study. However, the absorptions characters of minerals studied from USGS Spectral Library (Fig. 2) and the spectra measured over the field samples using PIMA spectrometer in the laboratory (Fig. 13 in Section 7), and the study of different rock units in the field are considered while selecting the ROI's.

In brief, the ML classification assumes that the statistics for each class in each band are normally distributed and calculates the probability that a given pixel belongs to a specific class (Jia and Richards, 1994; Richards and Jia, 2006; El Janati et al., 2014). Here, each pixel is assigned to the class that has the highest probability and each class relates to a pure endmember pixel. The extraction of common information is executed for the pure spectral components derived from reflectance spectral selection (Jia and Richards, 1994; Chen and Reed, 1987). SAM is a supervised classification algorithm based on statistical techniques and is dependent on the cluster identification of the image. The algorithm determines the spectral similarity between two spectra by calculating the angle between the spectra and treating them as vectors in a space with dimensionality equal to the number of bands (Yuhas et al., 1992; Kruse et al., 1993). Here, the smaller angles represent closer matches to the reference spectrum and the pixels further away than the specified maximum angle threshold in radians are not classified. SID is a spectral classification method that uses a divergence measure to match pixels to reference spectra. The smaller the divergence, the more likely the pixels are similar. Here, the pixels with a measurement greater than the specified maximum divergence threshold are not classified. SID improves the accuracy of the estimate of endmember abundance used in optimal classification (Xu and Zhao, 2008; El Janati et al., 2014).

Confusion matrixes of discussed image classification algorithms are carried out to the subset (503 × 603 pixels) of the study area. The results of matrixes are provided in the Table 4. Table 4 shows the best overall accuracy of 96.06% and the Kappa Coefficient of 0.95 produced by ML algorithm (Table 4a) while compare to the SAM and SID which are provided the overall accuracies of 57.02% and 62.44% and the Kappa Coefficients of 0.49 and 0.56 respectively (Table 4b and c). The ML algorithm distinctly identified all the rock formations of autochthonous units with the User's accuracy above 89.34% to the highest accuracy of 100% (Table 4a). The high overall accuracy of 96.06% is due to the presence of distinct compositions in different formations. The best result of the matrix of Maximum Likelihood algorithm is provided in Fig. 7. The Quaternary formations (Qdz, Qgy and Qmz) and sea water (Sw) of the study area were identified with the highest level accuracy of 100% that may be due to their simple and unique compositions. Both the black colored fusilinid–bearing limestone and dolomite, and schist and white tuff formations of the study area were identified with high level Producer's accuracy of 99% and User's accuracy around 98%. The dolerite sills and dykes, and calcareous schist and black limestone formations were identified with User's accuracies of 99.47% and 92.94% respectively. The dolerite sills and dykes are visible on the images (Figs. 2a, 5b, and 6) and the identification may be related to distinct igneous composition. The nodular limestone, yellow dolomite and silicified limestone bearing formation was produced User's accuracy of 89.34% which can be considered an accurately classified. The metamorphic rocks are easily distinguished from the associated carbonates formations of the area (Fig. 7). The minor occurrence of active or sub recent slope deposits and scree formations were assigned with the calcareous schist and black limestone formation. No significant larger commission and omission errors were noticed in the confusion matrix.

On the other hand, the SAM algorithm identified the black colored fusilinid–bearing limestone and dolomite distinctly with the high User's accuracy of 83.71% (Table 4b) in which, the dolerite sills and dykes, and the schist and white tuff formations were identified with User's accuracies of 70.81% and 68.71% respectively. The calcareous schist formations occurred with black limestone was identified with User's accuracy of 50.37%. The beach sands (Qmz) were identified with 61.29%. The other formations were poorly identified by the SAM algorithm. Similar to SAM, the SID algorithm identified the black colored fusilinid–bearing limestone and dolomite distinctly by the high User's accuracy of 83.41% (Table 4c). The dolerite sills and dykes, and the schist and white tuff formations were identified with User's accuracies of 78.77% and 74.16% respectively. The calcareous schist formations occurred with black limestone was identified with User's accuracy of 62.70%. All Quaternary formations were poorly identified. The identification of formations by the SID algorithm is relatively high and showed the overall accuracy of 62.44% compare to the SAM algorithm which produced the overall accuracy of 57.02%. It can be assessed that all algorithms identified the sea water with maximum accuracy of 100%. The ML and SID algorithms are better distinguished the formations rich in carbonates bearing limestone and dolomite, and the schists bearing metamorphic rocks of the study area by producing significant different User's accuracies to map such formations. In this study, ML algorithm seems most successful in clearly identifying all the formations and distinguishing the formations of autochthonous units. The interpretation of algorithms reveals that the most informative training targets and, ML with SID algorithms, can add more accuracy to map the distribution and the extent of metamorphic and carbonate formations.

The spectral bands of ASTER proved its capability to delineate metamorphic zone and to discriminate metamorphic rocks. The decorrelated and principal component

Please cite this article in press as: Rajendran, S., Nasir, S. Mapping of high pressure metamorphics in the As Sifah region, NE Oman using ASTER data. Adv. Space Res. (2014), http://dx.doi.org/10.1016/j.asr.2014.11.026

Table 4
Accuracy assessment matrix of ML, SAM and SID algorithms applied to the training lithological classes (Sq1Cs – calcareous schist, black limestone; $Sq2_a$ - black, fusilinid –bearing limestone and dolomite; Sq_1L – nodular limestone, yellow dolomite, silicified limestone; Sq1V – schist and white tuff; SqDI – dolerite sills and dykes; Qgy-Sub-recent alluvial fans, terraces; Qdz – coastal dunes; Qmz – beach sand; Sw – sea water).

Class	Sq1Cs	Sw	Qdz	$Sq2_a$	Sq_1L	Sq1V	SqDI	Qgy	Qmz	Total	User's accuracy
a. Accuracy assessment matrix of ML algorithm											
Unclassified	0.00	0.00	0.00	0.00	0.00	0.00	0.00	0.00	0.00	0.00	
Sq1Cs	93.32	0.00	0.00	0.67	10.64	0.00	0.52	0.00	0.00	24.29	92.94
Sw	0.00	100.00	0.00	0.00	0.00	0.00	0.00	0.00	0.00	3.26	100.00
Qdz	0.00	0.00	100.00	0.00	0.00	0.00	0.00	0.00	0.00	1.93	100.00
$Sq2_a$	0.56	0.00	0.00	99.11	0.24	0.00	0.00	0.00	0.00	15.20	98.88
Sq_1L	6.12	0.00	0.00	0.22	89.13	0.00	0.00	0.00	0.00	14.31	89.34
Sq1V	0.00	0.00	0.00	0.00	0.00	99.45	2.09	0.00	0.00	18.93	97.85
SqDI	0.00	0.00	0.00	0.00	0.00	0.55	97.38	0.00	0.00	19.03	99.47
Qgy	0.00	0.00	0.00	0.00	0.00	0.00	0.00	100.00	0.00	1.83	100.00
Qmz	0.00	0.00	0.00	0.00	0.00	0.00	0.00	0.00	100.00	1.02	100.00
Total	100.00	100.00	100.00	100.00	100.00	100.00	100.00	100.00	100.00	100.00	
Producer's accuracy	93.32	100.00	100.00	99.11	89.13	99.45	97.38	100.00	100.00		
Overall accuracy = 96.06%; Kappa Coefficient = 0.95											
b. Accuracy assessment matrix of SAM algorithm											
Unclassified	0.00	3.13	0.00	0.00	0.00	0.00	0.00	0.00	3.33	0.14	
Sq1Cs	18.92	0.00	0.00	0.67	16.31	7.83	1.75	12.96	6.67	9.16	50.37
Sw	0.00	96.88	0.00	0.00	0.00	0.00	0.00	0.00	0.00	3.15	100.00
Qdz	6.95	0.00	70.18	2.01	15.84	0.91	0.17	0.00	10.00	5.94	22.86
$Sq2_a$	4.45	0.00	15.79	83.89	5.20	1.82	0.00	0.00	0.00	15.20	83.71
Sq_1L	28.93	0.00	12.28	8.95	39.95	6.01	1.22	0.00	0.00	15.74	36.42
Sq1V	7.93	0.00	1.75	4.47	10.87	59.20	4.19	0.00	0.00	16.04	68.71
SqDI	11.13	0.00	0.00	0.00	3.55	17.85	83.42	1.85	10.00	22.90	70.81
Qgy	21.14	0.00	0.00	0.00	6.86	6.38	8.90	85.19	6.67	10.69	14.60
Qmz	0.56	0.00	0.00	0.00	1.42	0.00	0.35	0.00	63.33	1.05	61.29
Total	100.00	100.00	100.00	100.00	100.00	100.00	100.00	100.00	100.00	100.00	
Producer's accuracy	18.92	96.88	70.18	83.89	39.95	59.20	83.42	85.19	63.33		
Overall accuracy = 57.02%; Kappa Coefficient = 0.49											
c. Accuracy assessment matrix of SID algorithm											
Unclassified	0.00	0.00	0.00	0.00	0.00	0.00	0.00	0.00	0.00	0.00	
Sq1Cs	27.12	0.00	0.00	0.00	18.44	3.64	1.92	3.70	16.67	10.55	62.70
Sw	0.00	100.00	0.00	0.00	0.00	0.00	0.00	0.00	0.00	3.26	100.00
Qdz	7.09	0.00	57.89	6.49	8.98	0.55	0.17	0.00	3.33	5.29	21.15
$Sq2_a$	6.26	0.00	22.81	84.34	3.31	0.55	0.00	0.00	0.00	15.33	83.41
Sq_1L	23.09	0.00	12.28	4.25	46.34	0.00	1.05	0.00	6.67	13.43	49.49
Sq1V	6.54	0.00	7.02	4.92	10.64	72.68	3.49	1.85	0.00	18.25	74.16
SqDI	6.12	0.00	0.00	0.00	3.78	11.84	82.90	1.85	6.67	20.45	78.77
Qgy	20.86	0.00	0.00	0.00	2.84	10.75	9.95	92.59	0.00	11.13	15.24
Qmz	2.92	0.00	0.00	0.00	5.67	0.00	0.52	0.00	66.67	2.31	29.41
Total	100.00	100.00	100.00	100.00	100.00	100.00	100.00	100.00	100.00	100.00	
Producer's accuracy	27.12	100.00	57.89	84.34	46.34	72.68	82.90	92.59	66.67		
Overall accuracy = 62.44%; Kappa Coefficient = 0.56											

images studied are successful in providing useful informations on the occurrence and distribution of metamorphic rock types. However, the resulted images of both the image processing method were not able to provide informations on the minerals of the formations and thus, an attempt is made here to use the SAM spectral analysis to provide more informations on the occurrence of major minerals of the formations as described below.

6.4. Detection of metamorphic minerals

To identify the minerals of metamorphic schists that contain predominantly the OH molecules and the minerals of limestone and dolomite formations that contain more CO_3 contents in each pixel of image of the study region (Fig. 2), and to confirm the occurrence of metamorphic rocks of the region, we applied the Spectral Angle Mapper (SAM) spectral analysis method working based on the "Spectral Hourglass" scheme (Kruse et al., 2003; Gabr et al., 2010; Rajendran et al., 2013; Rajendran and Nasir, 2014c) available in ENVI 5 image processing and analysis software (http://www.exelisvis.com) to the study region. The method is one of the widely accepted popular image processing techniques for hyperspectral image processing, which can also be used in lower spectral resolution systems (Kruse et al., 1993; Rowan and Mars, 2003; Gabr et al., 2010; Rajendran et al., 2013; Rajendran and Nasir, 2014c). The hyperspectral tools (MNF, PPI and *n*-Dimensional viewer) applied on the nine ASTER VNIR–SWIR spectral bands of the study region initially determined the

Please cite this article in press as: Rajendran, S., Nasir, S. Mapping of high pressure metamorphics in the As Sifah region, NE Oman using ASTER data. Adv. Space Res. (2014), http://dx.doi.org/10.1016/j.asr.2014.11.026

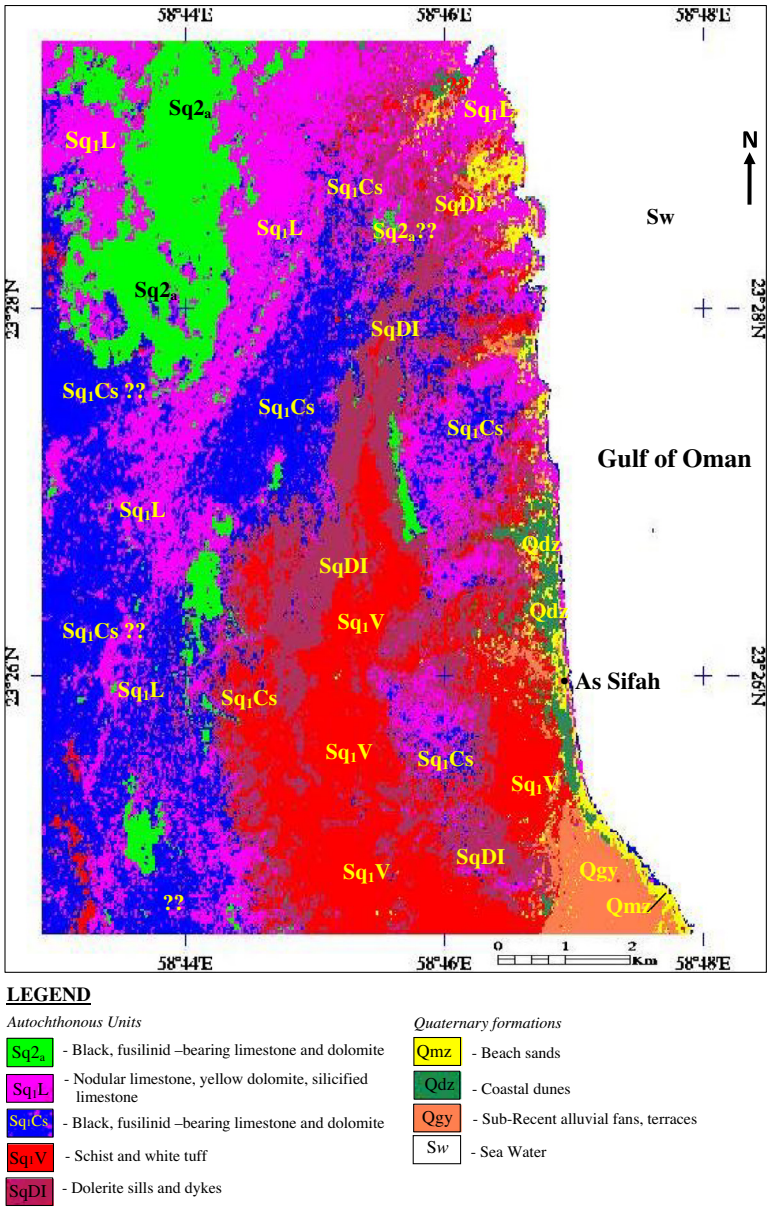

Fig. 7. The classified image of matrix of the Maximum Likelihood algorithm shows the occurrence of metamorphic rocks and carbonates formations in the As Sifah region.

inherent dimensionality of MNF image data (Boardman and Kruse, 1994) consist increase of noise from MNF bands 1–9. These bands are further processed to determine the most spectrally pure (extreme) pixels, contains mineral information of the image by PPI providing the PPI iteration value of 10,000 (the maximum), the default threshold value of 2.5 and the SAM angle of 0.16 in radians. The values set at the SAM procedure classified the entire pixels (273,308 pixels of total area of 61.49 Km^2) of the image. The obtained pure pixels in the image were typically corresponding to the mixing endmembers computed by repeatedly projecting *n*-D scatter plots on a random unit vector. Fig. 8 shows the spectra (*n*-D class Mean) derived based on endmembers. Table 5 provides the detail on number of pixels which are classified with their relative percentages and the total area of their distribution in the study region. Fig. 9 is the SAM classified image shows the occurrence and spatial distribution of different minerals that are occurred in various proportions in different rock types (annotated to the interest of readers of the paper) of the study region with respective colors of the *n*-D class Mean spectra. The SAM image can be compared and better studied using the geological map (Fig. 2b) and the classified images (Figs. 4, 6 and 7) discussed above. More details on the processing of image and absorption characters of *n*-D class Mean spectra can be found in Rajendran et al. (2013) and Rajendran and Nasir (2014c).

The SAM image (Fig. 9) shows the classified pixels mainly in the four *n*-D classes viz. *n*-D class #1, *n*-D class #2, *n*-D class #3 and *n*-D class #5. The mean spectra of

Please cite this article in press as: Rajendran, S., Nasir, S. Mapping of high pressure metamorphics in the As Sifah region, NE Oman using ASTER data. Adv. Space Res. (2014), http://dx.doi.org/10.1016/j.asr.2014.11.026

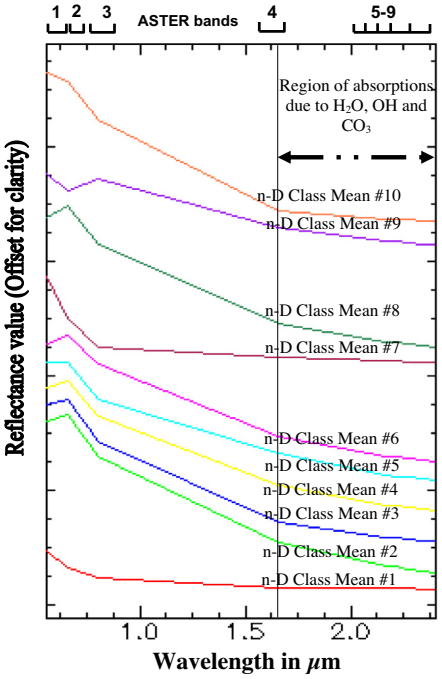

Fig. 8. The plot of end member spectra (Class Means) of As Sifah region.

Table 5
Distribution of pixels of As Sifah region in the SAM n-D classes.

n-D Classes[a]	No. of pixels	% in total area	Area in Km^2
n-D class Mean #1	59469	21.759	13.3805
n-D class Mean #2	43284	15.837	9.7389
n-D class Mean #3	66007	24.151	14.8515
n-D class Mean #4	340	0.124	0.0765
n-D class Mean #5	98192	35.927	22.0932
n-D class Mean #6	406	0.149	0.0913
n-D class Mean #7	3449	1.262	0.7760
n-D class Mean #8	430	0.157	0.0967
n-D class Mean #9	79	0.029	0.0177
n-D class Mean #10	1652	0.604	0.3717
Total	273,308	99.99	61.4943

[a] Unclassified: 0 points (0.000%) (0.0000 km^2).

n-D class #1 (Fig. 8) shows flat strong absorption almost entire wavelength of ASTER spectral bands of VNIR–SWIR regions from band 1 (0.52–0.60 μm) to band 9 (2.36–2.43 μm). The pixels of classified based on *n*-D class #1 (red in color) provided the 13.3805 km^2 area found in the region of Gulf of Oman and along the wadi flows near to the location of As Sifah (Fig. 9). The classification is due to presence of water molecules and chlorophyll contents (Rajendran et al., 2013; Rajendran and Nasir, 2014c) in the features. The spectra not showing any distinct absorption in visible or infrared region may be due to stretching of bands characteristics to predominant occurrence of water and hydroxyl molecules in the features. The Gulf of Oman and the area of vegetations were confirmed in the ASTER RGB (3, 2 and 1) image (Fig. 2a) and validated during the field check. The occurrence and spatial distribution of carbonate minerals namely calcites are detected about

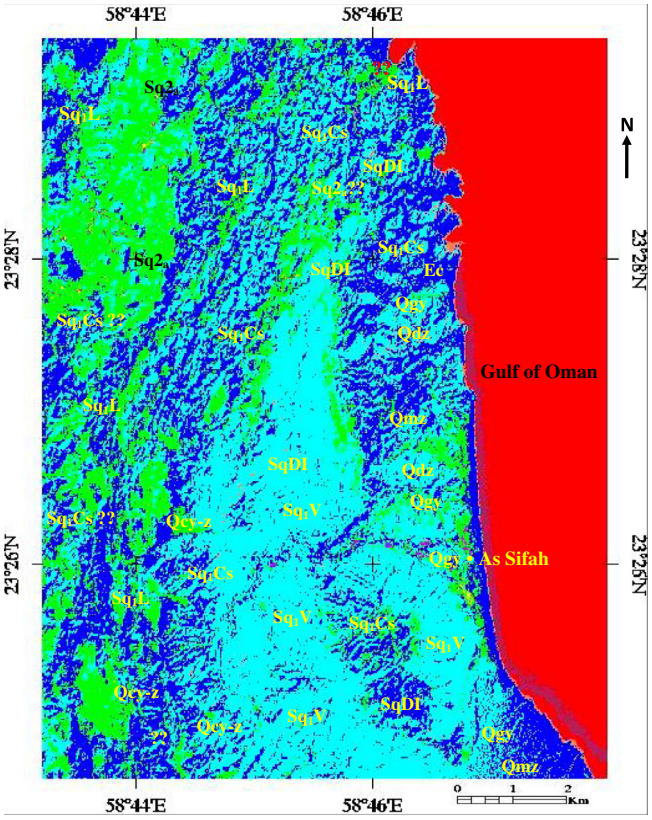

Fig. 9. SAM classified image shows the occurrence and spatial distribution of hydroxyl bearing silicates (in cyan color) and carbonates (in green and blue colors) minerals (Qmz – beach sand; Qcz – coastal dunes; Qcy-z – active or sub recent slope deposits, scree; Qgy – sub-Recent alluvial fans; terraces; S_q2_a – black, fusilinid–bearing limestone and dolomite; S_{q1}VL – nodular limestone, yellow dolomite, silicified limestone; S_{q1}Cs – calcareous schist, black limestone; S_{q1}V – schist and white tuff; SqDI – dolerite sills and dykes). (For interpretation of the references to color in this figure legend, the reader is referred to the web version of this article.)

9.7389 km^2 in green color by *n*-D class #2 and dolomites are detected about 14.8515 km^2 in blue color by *n*-D class #3. The extracted endmember spectra of n-D class #2 and *n*-D class #3 shows strong absorptions around 2.3 μm (compare the reflectance differences among the mean spectra) due to the presence of calcium and magnesium carbonate minerals that are occurred on the surface of rocks (Rajendran et al., 2013). The occurrence of such pixels are observed more in the place of black colored fusilinid limestone and dolomite, the calcareous schist with black limestone, and the formations consist of nodular limestone, yellow dolomite and silicified limestone. The occurrences of magnesium carbonates (14.8515 km^2) are more than the calcium carbonates (9.7389 km^2) in the region (Fig. 9). The occurrence of calcium carbonates is found more in the formations of black colored fusilinid limestone and dolomite.

The image classified the occurrence and spatial distribution of minerals of amphibole, mica and chlorite groups in yellow color by the *n*-D class #4 about 0.0765 km^2 and in cyan color by the *n*-D class #5 about 22.0932 km^2. Both the spectra (Fig. 8) show absorptions from 1.4 to

Please cite this article in press as: Rajendran, S., Nasir, S. Mapping of high pressure metamorphics in the As Sifah region, NE Oman using ASTER data. Adv. Space Res. (2014), http://dx.doi.org/10.1016/j.asr.2014.11.026

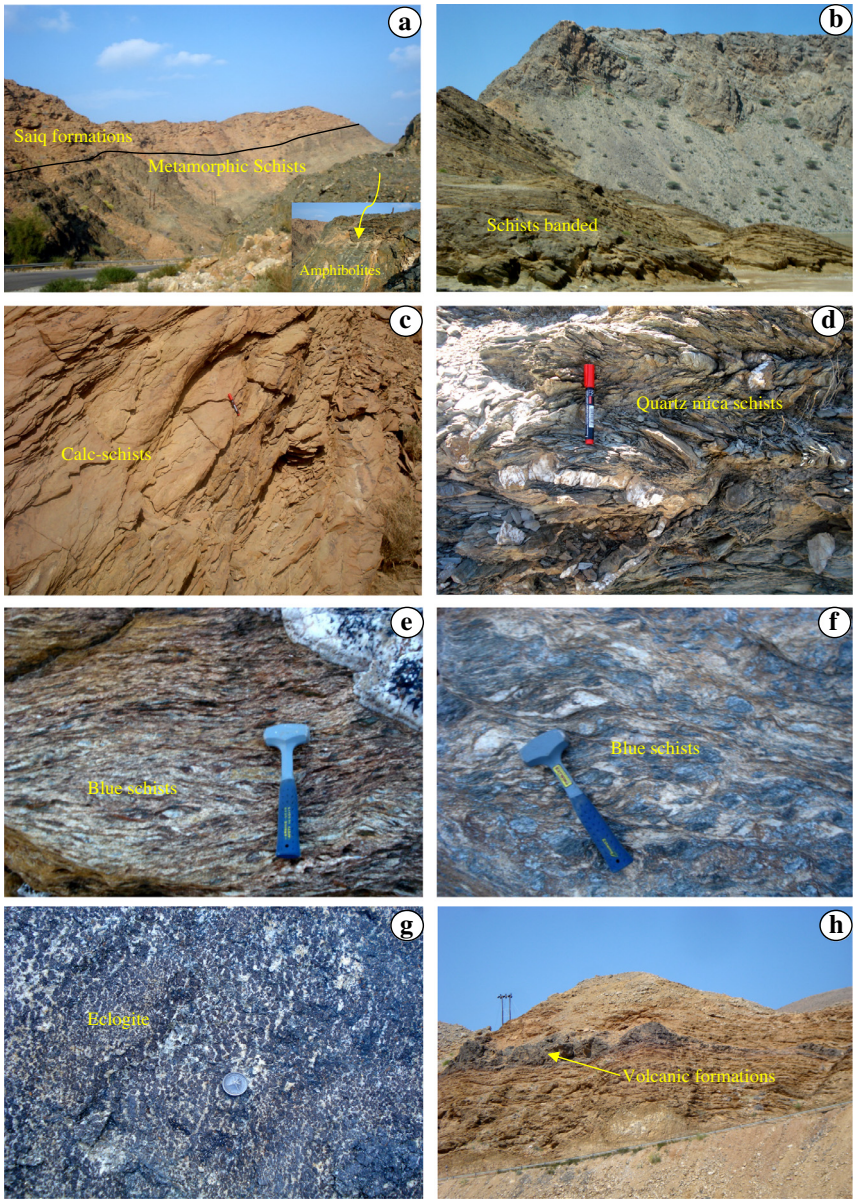

Fig. 10. Field photographs show the occurrence of (a) carbonate formations and amphibolites, (b) thick banded schists, (c) calcareous schists, (d) quartz mica schists, (e) and (f) blue schists, (g) eclogite and (h) the occurrence of volcanic formations in and around of the As Sifah region. (For interpretation of the references to color in this figure legend, the reader is referred to the web version of this article.)

2.43 μm. The study of reflectance values of these pixels show relatively high values compare to the reflectance values of pixels of carbonates. The classification is due to the absorption of hydroxyl molecules present in the group of minerals (Rajendran and Nasir, 2014c). The distribution of pixels in cyan color are found more (22.0932 km^2) in the regions occurred with the schist and white tuff and calcareous schist with black limestone. The occurrence and distribution of pixels in the region represents the presence of OH bearing aluminosilicate minerals (Rajendran and Nasir, 2014c). The area detected by these minerals can be compared with the regions occurred in the ASTER decorrelated image (Fig. 4) and principal components image (Fig. 6). The occurrence of such minerals in the carbonate formations may be due to presence of interlayered clays in the formations. The other *n*-D classes, from *n*-D class #6 to *n*-D class #10, are not showing any significant concentration of pixels and more occurrences of other minerals in the study region (Rajendran et al., 2013; Rajendran and Nasir, 2014c). Thus, the occurrence of formations of the study region are classified by the SAM image mainly into carbonates and schists by the presence of principal minerals such as calcite and dolomite in the carbonate formations and the OH bearing metamorphic minerals in the schists. The region of metamorphic zone and the metamorphic rocks that occurred mainly with schists are confirmed by presence of the OH bearing metamorphic minerals through the SAM method.

Please cite this article in press as: Rajendran, S., Nasir, S. Mapping of high pressure metamorphics in the As Sifah region, NE Oman using ASTER data. Adv. Space Res. (2014), http://dx.doi.org/10.1016/j.asr.2014.11.026

7. Field and laboratory studies

To evaluate the sensor capability of ASTER that delineated the metamorphic zone and discriminated metamorphic rocks from the carbonate formations, and to confirm the occurrences of the minerals and rock types in the study region, we carried out field verifications with existing geological maps and interpreted satellite images. The fieldworks are confirmed in showing the existent lithologies and occurrence of carbonate and OH bearing metamorphic minerals in the region as interpreted in the remotely sensed imagery. The field observations and studies of field samples in the laboratories are agreed well with the field descriptions provided by the earlier workers.

7.1. Field studies

More details about the geology, petrography, geochemistry, metamorphism and thermo barometric studies of rock units of the metamorphic and carbonate rocks of the region can be referred in Michard et al. (1984), Goffé et al. (1988), El-Shazly and Coleman (1990), El-Shazly et al. (1990, 1994, 1997), Searle et al. (1994, 2004), El-Shazly (1995), Gregory et al. (1998), Miller et al. (1999, 2002), Gray et al. (2000, 2005) and Searle and Cox (2002). Several research studies are carried out in selected areas around the As Sifah region. During the field work, the occurrence of calcareous schists, quartzofeldspathic mica schists, metapelites rocks in metamorphic zone are observed. All the rock types are appeared as metamorphosed equivalents of the Late Permian Saiq Formation shelf facies sediments occurred with minor doleritic sills, volcanic horizons and ash-flow tuffs (Le Métour et al., 1986; El-Shazly et al., 1997). The metamorphic grade of the region increases from west to east (El-Shazly et al., 1990). Samples were collected from different outcrops of calcareous schists, quartz mica schists, blueschists and epidote amphibolites and eclogites. All are representative of blue schist and eclogite facies metamorphic rocks. The recrystallized meta-sedimentary rocks namely marble, radiolarian chert and shale are also observed.

In field, the fusilinid bearing limestone and dolomite, and nodular limestone are massive and friable. The dolomite rocks are highly fractured and friable interlayered by thin layers of shale. The schists are underlined the carbonate formations (Fig. 10a) and are intermixed with amphibolites (inset in Fig. 10a). Thick banded calcareous schists (Fig. 10b) are exposed at the upper part of the greenschists.

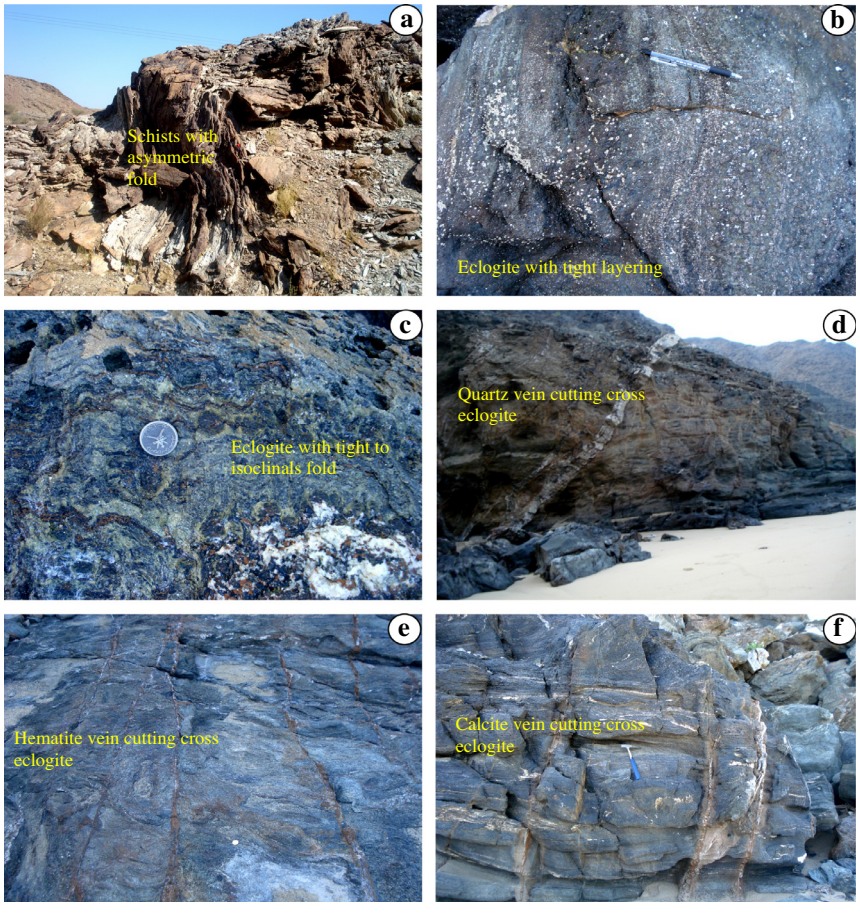

Fig. 11. Field photographs show the occurrence of (a) asymmetric folds in schists, (b) and (c) tight and isoclinals fold in eclogites, (d)–(f) the late stage veins of quartz, hematite and calcite cutting cross the eclogite found in and around of the As Sifah region.

Please cite this article in press as: Rajendran, S., Nasir, S. Mapping of high pressure metamorphics in the As Sifah region, NE Oman using ASTER data. Adv. Space Res. (2014), http://dx.doi.org/10.1016/j.asr.2014.11.026

The calc-schists (Fig. 10c) are the metamorphosed Saiq Formation dolomite, and the quartz mica schists (Fig. 10d) are of metamorphosed quartzites of Amdeh Formation (Miller et al., 2002; Searle et al., 2004). The dolomite rocks of Saiq Formation are occurred with reef corals (Le Métour et al., 1986). These rocks contain carpholite. The blueschists (Fig. 10e and f) consist of garnet + glaucophane + phengite and the eclogites (Fig. 10g) are found in the lower part of region. These are belonging to the metamorphosed Saiq 1 volcanic formations (Fig. 2b, 10 h; El-Shazly et al., 1994; Searle et al., 1994, 2004). Systematic downward increase in metamorphic grades and the occurrence of high-grade mineral assemblages with garnet and clinopyroxene minerals are observed. The schistosity and compositional banding are deformed by ductile, tight to isoclinal asymmetric folds (Fig. 11a). Fig. 11b and c show the style of the tight to isoclinal folds in the eclogites. The occurrence of eclogites within glaucophane schists (blueschists) are observed along the coastal section of As Sifah (Le Métour et al., 1986; Goffé et al., 1988; El-Shazly et al., 1990). The eclogite layers are concordantly interfolded with calcareous and phengite-rich schists. The green schists and garnet-free blueschists are interlayered within the eclogites and garnet blueschists. Late stage quartz, hematite and calcite veins (Fig. 11d–f) are ubiquitous and cutting the eclogites. The mafic rocks contain segregation of lined garnets, clinopyroxenes or amphiboles.

7.2. Laboratory studies

7.2.1. Microscopic study

Forty-two microscope thin sections were prepared to study the minerals of the rocks of the study area. Under the microscope, the samples of carbonate formation consists fusilinid bearing calcite and dolomite. The schists exhibit a variety of mineral assemblages (El-Shazly et al., 1990, 1994, 1997; Searle et al., 1994, 2004; Miller et al., 2002). The calcareous schist (Fig. 12a) consists mainly of calcite, phengite chlorite, muscovite, illite and quartz with minor occurrences of paragonite, magnetite or hematite. The quartz rich mica schist (Fig. 12b) shows the presence of quartz, muscovite, paragonite, phengite, chlorite, illite and albite with accessories of magnetite and apatite. The epidote amphibolite rock (Fig. 12c) consists of epidote, albite, hornblende, chlorite and phengite. The accessories are magnetite, hematite and apatite. The occurrence of two generations of blue amphibole can be distinguished by their colour zoning (inset in Fig. 12c). Stage-I amphiboles have darker cores and pale rims, whereas second stage crossites have cores with darker colors. The blueschist (Fig. 12d) consists of glaucophane, epidote, garnet, phengite, illite and quartz with minor amount of rutile and apatite (El-Shazly et al., 1990). Glaucophane was partially replaced by biotite, or pseudomorphed by chlorite + albite, whereas phengite was rimmed by biotite

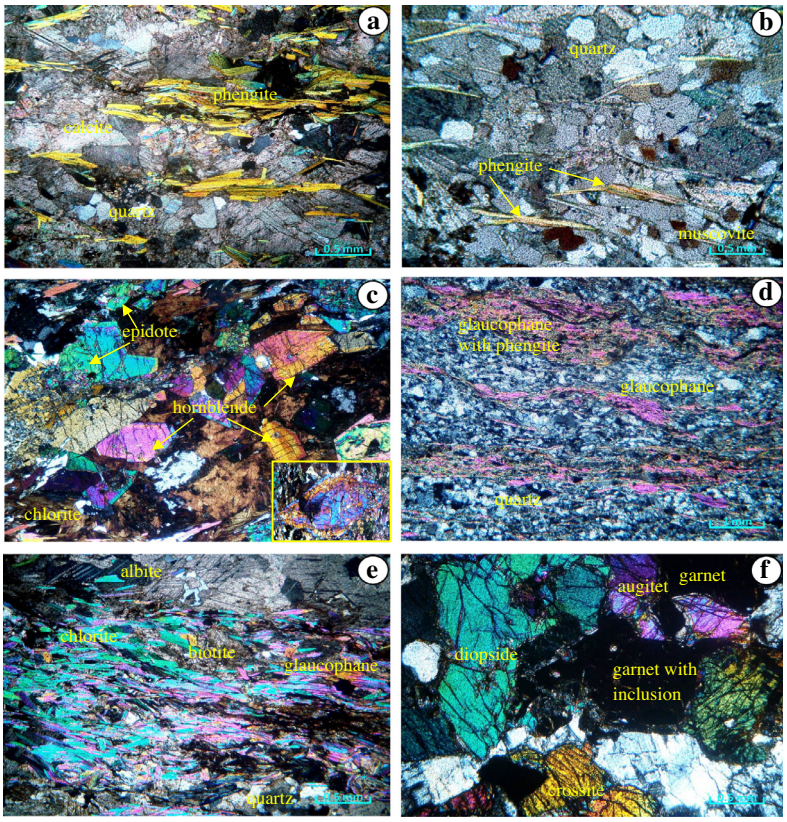

Fig. 12. Photomicrographs (nicols crossed) show the occurrence of major minerals in (a) the calcareous schist, (b) the quartz mica schist, (c) the epidote amphibolite rock, (d) and (e) the glaucophane blue schist, and (f) the eclogite of the As Sifah region. (For interpretation of the references to color in this figure legend, the reader is referred to the web version of this article.)

Please cite this article in press as: Rajendran, S., Nasir, S. Mapping of high pressure metamorphics in the As Sifah region, NE Oman using ASTER data. Adv. Space Res. (2014), http://dx.doi.org/10.1016/j.asr.2014.11.026

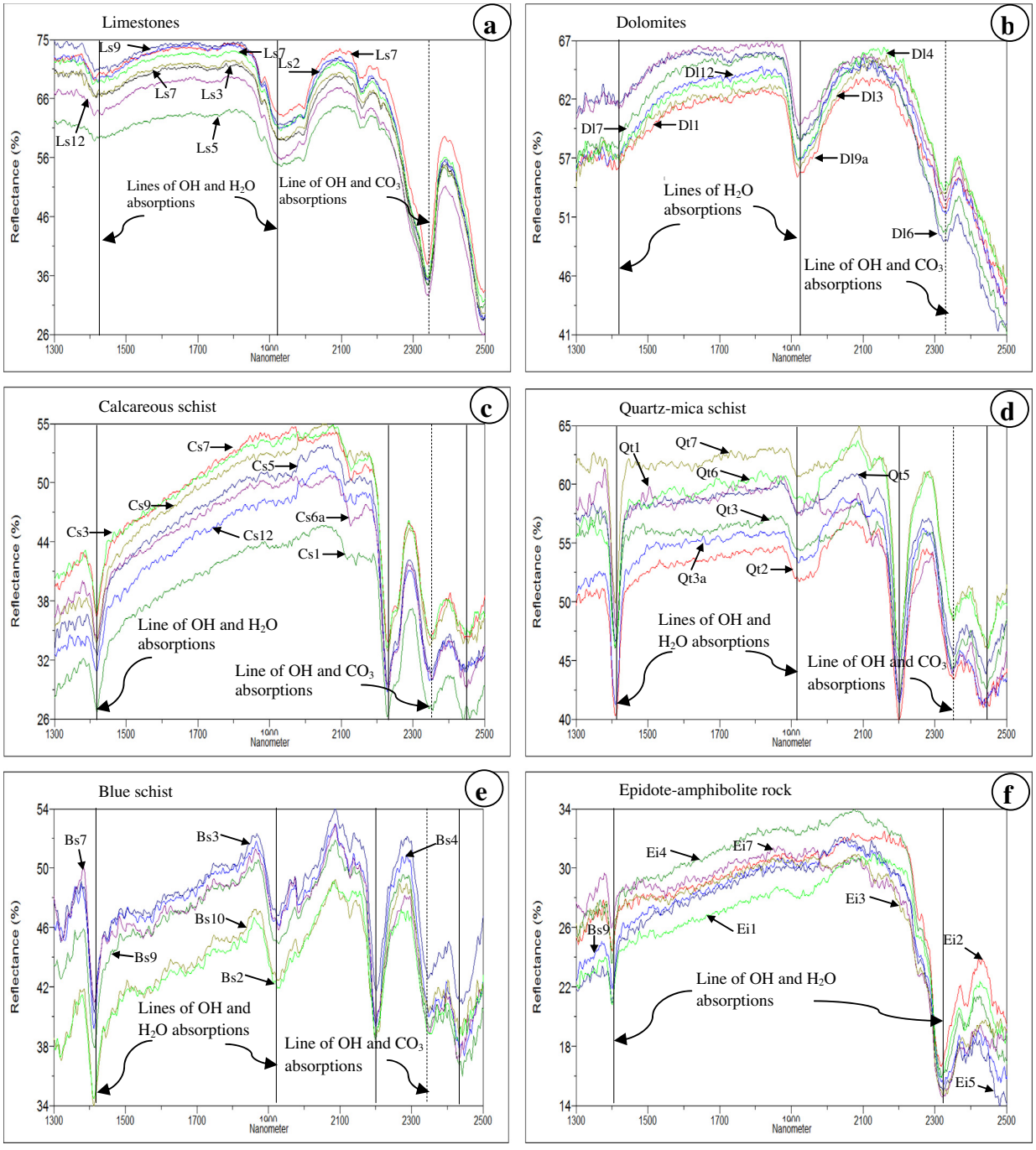

Fig. 13. PIMA spectral plots shows the absorptions regions of (a) calcite of fusilinid bearing limestone (S_q2_a) and nodular limestone rocks (Sq_1L), (b) dolomite of dolomite (S_q2_a) and yellow dolomite (Sq_1L) rocks, (c) phengite of calcareous schists (Sq_1Cs), (d) muscovite of quartz mica schists (Sq_1V), (e) glaucophane of blue schists (Sq_1V), and (f) hornblende in epidote–amphibolite rock of the As Sifah region. (For interpretation of the references to color in this figure legend, the reader is referred to the web version of this article.)

(Fig. 12e). Eclogite (Fig. 12f) consists of garnet, clinopyroxene, glaucophane, epidote, phengite and quartz. Minerals within the eclogite contain abundant inclusion and retrograded epidote (Searle et al., 1994). The minerals are included in garnet which may have been generated by fracturing and extension. The earlier generation of the minerals such as clinopyroxene, crosstie and phengite are polygonized around microfolds. At some places, the garnet in eclogites is progressively replaced by epidote + chlorite.

7.2.2. Spectral study

More than 350 spectral measurements of rocks have been taken using the portable PIMA SP infrared spectrometer at different locations in the field and over the samples in the laboratory to study the spectral absorption characters of carbonate and metamorphic rocks. The spectra collected over the different rock types confirm the presence of carbonate bearing minerals namely calcite and dolomite in the limestone and dolomitic rocks, and OH bearing

Please cite this article in press as: Rajendran, S., Nasir, S. Mapping of high pressure metamorphics in the As Sifah region, NE Oman using ASTER data. Adv. Space Res. (2014), http://dx.doi.org/10.1016/j.asr.2014.11.026

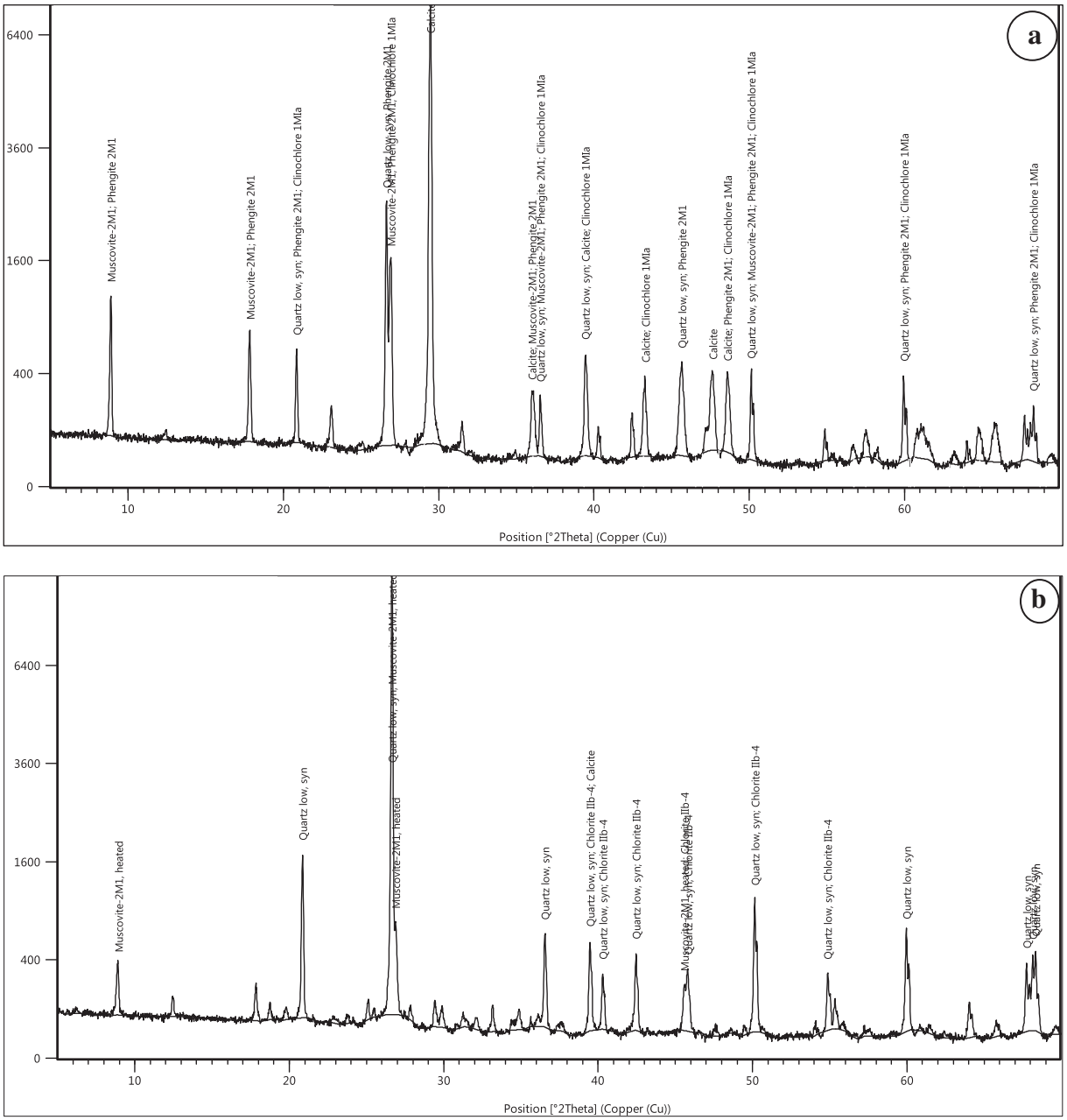

Fig. 14. (a) and (b) Results of XRD analyze of (a) calcareous schist and (b) quartz mica schist rocks. c–d results of XRD analyze of (c) glaucophane schist and (d) epidote amphibolite rocks.

minerals such as phengite, paragonite, glaucophane, chlorite, epidote and hornblende in the different metamorphic rocks (Fig. 13a–f). The spectra of fusilinid bearing limestone and nodular limestone rocks, and dolomite and yellow dolomite rocks of carbonate formations are given in Fig. 13a and b respectively. The spectra of limestone and dolomite rocks clearly show the absorptions near 1400 nm, 1900 nm (solid line, Fig. 13a and b), and 2300 nm (dashed line, Fig. 13a and b). The light absorptions near 1400 nm and broad absorptions at 1900 nm are due to OH bearing silicate minerals in the rocks. The deep and strong absorptions in limestone rocks and shallow absorptions in dolomite rocks near 2300 nm are due to presence of CO_3 contents in the minerals calcite and dolomite (Hunt, 1977; Rajendran et al., 2013; Rajendran and Nasir, 2014c) in the rocks. The broad absorption in limestone and deep absorptions in dolomite rocks near 1900 nm may also attributes the presence of the calcium and magnesium contents respectively in the carbonate minerals.

The spectra of calcareous schist and quartz muscovite schist rocks are given in Fig. 13c and d respectively. Calcareous schist is composed of the major minerals calcite, phengite, chlorite, illite and quartz, while the quartz mica schist contains the minerals quartz, phengite, paragonite, chlorite, illite and albite. The spectra of calcareous

Please cite this article in press as: Rajendran, S., Nasir, S. Mapping of high pressure metamorphics in the As Sifah region, NE Oman using ASTER data. Adv. Space Res. (2014), http://dx.doi.org/10.1016/j.asr.2014.11.026

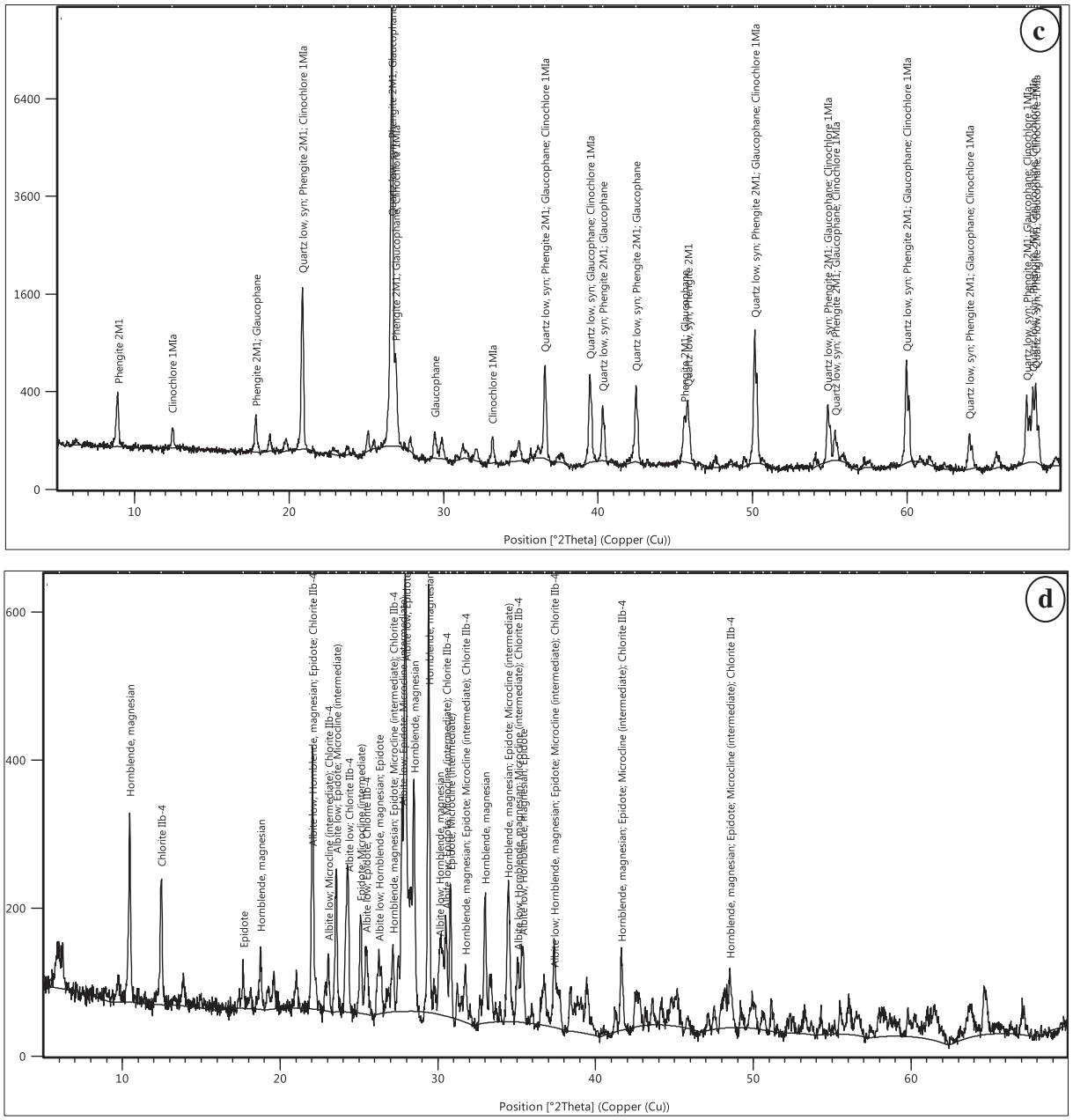

Fig 14. *(continued)*

schist (Fig. 13c) show absorptions near 1400, 2200, 2350 and 2450 nm. The absorptions near 1400 nm is due to presence of OH contents, and the deep strong absorptions at 2200 nm attributes the presence of Al–OH molecules and Mg, Fe, Ca contents in the hydrous silicate minerals. The absorptions near 2350 nm are due to presence of CO_3 in calcite and the absorptions at 2450 nm due to Al–OH in illite minerals (Clark et al., 1990; Chabrillat and Goetz, 2006). The spectra collected over the quartz rich muscovite schists show absorptions near 1900 nm in addition to the absorption regions of calcareous schists. The broad absorption occurred near 1900 nm is due to presence of water and hydroxyl molecules in the hydrous silicate minerals. The poor absorptions near 2350 and 2450 nm may be due to the stretching of Mg–OH and Al–OH molecules.

The blueschist consists mainly of glaucophane, epidote, garnet, phengite, chlorite and illite. The spectra collected over the rocks (Fig. 13e) shows absorptions near 1400, 1900, 2200, 2350 and 2450 nm similar to muscovite schists. The deep and strong absorptions near 1400 nm and broad absorptions near 1900 nm are due to presence of OH molecules in glaucophane, epidote and other OH bearing silicate minerals. As well as the deep and strong absorptions at 2200 nm attribute the presence of Al–OH molecules and Mg, Fe, Ca, Na contents in glaucophane, epidote and phengite. The poor absorptions near 2350 nm are due to stretching of Mg–OH molecules and the absorptions

Please cite this article in press as: Rajendran, S., Nasir, S. Mapping of high pressure metamorphics in the As Sifah region, NE Oman using ASTER data. Adv. Space Res. (2014), http://dx.doi.org/10.1016/j.asr.2014.11.026

near 2450 nm may be due to Al–OH in illite. The epidote amphibolite rock shows the occurrence of epidote, albite, hornblende, chlorite and phengite minerals. The spectra of the rocks (Fig. 13f) show absorptions at 1400 nm and near to 2300 nm. The absorptions near 1400 nm are due to presence of OH molecules and the absorptions near to 2300 nm are due to Mg–OH molecules in epidote, hornblende and phengite.

Overall, it is interesting to interpret the spectra of carbonate and metamorphic rocks. The collection of spectra in the SWIR region with a spectral resolution of 7 nm show absorption features mainly near to 1400 nm, 1900 nm, 2200 nm, 2300 and 2450 nm which are all due to presence of the H_2O, OH, Al–OH, Mg–OH and CO_3 molecules occurred in different proportions in the minerals of the rocks. The spectra are well correlatable with the spectra of Fig. 3 and their characters discussed in Section 3. The spectra of the metamorphic schists, that contains OH bearing silicate minerals, have strong absorptions near 1400 and 1900 nm due to OH molecules, and 2200 nm due to Al–OH. The phengite rich calcareous schists have absorptions near 1400 and 2200 nm, whereas the quartz muscovite schists have relative strong absorptions near 1400, 1900 and 2200 nm which depends on the different composition and amount of OH and Al–OH molecules in the silicate minerals. The spectra of quartz mica schists are similar to blueschists. But, blueschists show more deep absorptions near 1900 nm and relatively less absorptions near 2200. The differences in absorption are due to the distribution of OH and Al–OH contents in glaucophane, epidote, chlorite and phengite minerals. The epidote amphibolite rocks do not have much amount of OH molecules (weak absorption at 1400 nm) compare to other schist rocks and show strong absorptions near 2300 nm which are due to the presence of Mg–OH molecules in the minerals. The occurrences of such minerals in the rocks are confirmed by XRD analyses (Fig. 14). The plot of calcareous schist confirms the occurrence of major minerals such as calcite, phengite chlorite, muscovite and quartz (Fig. 14a). The plot of quartz-mica schist shows the occurrence of quartz, muscovite, paragonite, phengite and chlorite (Fig. 14b). The plot of glaucophane schist shows the presence of glaucophane, epidote, garnet, phengite, illite and quartz (Fig. 14c), and the plot of epidote amphibolite rock shows the presence of hornblende, epidote, albite and chlorite minerals (Fig. 14d).

8. Conclusion

In this study, the high pressure metamorphic zone and associated rock formations of As Sifah region of NE Oman are mapped using VNIR–SWIR spectral bands of ASTER by decorrelation stretching and PCA image processing methods by studying spectral properties of minerals. The image of decorrelated ASTER spectral bands 5, 6 and 8 showed the region of high pressure metamorphic zone and the image of principal components (PC4, PC3 and PC2) discriminated the different rocks associated with the metamorphic zone. The study of accuracy assessment on the occurrence and spatial distribution of major rocks in the geologic remote sensing showed the absorption capability of ASTER spectral bands and the image processing methods employed and recommends ML, SAM and SID algorithms to similar region having inherent geologic character of the earth surface. The occurrences of different formations are further confirmed by detection of their principal minerals using SAM spectral analysis. The image interpretations are verified in the field and checked for their occurrences. The mineralogy of the different rock formations are further confirmed under microscope studies, XRD analysis and PIMA spectral measurements in the laboratory. The study proved the sensor capability of ASTER in delineation of metamorphic zone and discrimination of metamorphic rock types. Therefore, the technique is recommended to geologists to map metamorphic zones and associated metamorphic rock types occurred in the rugged topography in similar arid region.

Acknowledgments

The authors are thankful to the NASA Land Processes Distributed Active Archive Center User Services, USGS Earth Resources Observation and Science (EROS) Center (https://LPDAAC.usgs.gov) for providing the ASTER data. The study is supported by Sultan Qaboos Internal Grant IG/SCI/ETHS/14/02. The XRD analytical help is extended by Mr. Saif Amer Al-Maamari, (CAARU, SQU) and the help extended for the preparation of micro thin sections by Mr. Hamdan Saif Al-Zidi and Mr. Bader Al Wali, the technicians, Department of Earth Sciences, SQU are thankfully acknowledged. The authors are thankful to the editor of the journal and the anonymous reviewers of the paper for their valuable reviews and providing useful comments and suggestions that have helped to present the work lucidly.

References

Abdeen, M.M., Allison, T.K., Abdelsalam, M.G., Stern, R.J., 2001. Application of ASTER band ratio images for geological mapping in arid regions; the neoproterozoic Allaqi Suture, Egypt. Geol. Soc. Am. Abstr. Prog. 3 (3), 289.

Abdelsalam, M.G., Stern, R.J., Berhane, W.G., 2000. Mapping gossans in arid regions with Landsat TM and SIR-C images: the Beddaho alteration zone in Northern Eritrea. J. Afr. Earth Sci. 30 (4), 903–916.

Abrams, M.J., Hook, S.J., 1995. Simulated ASTER data for geologic studies. IEEE Trans. Geosci. Remote Sens. 33, 692–699.

Abrams, M.J., Rothery, D.A., Pontual, A., 1988. Mapping in the Oman ophiolite using enhanced landsat thematic mapper images. Tectonophysics 151, 387–401.

Adams, J.B., 1974. Visible and near-infrared diffuse reflectance-spectra of pyroxenes as applied to remote sensing of soil objects in the solar system. J. Geophys. Res. 79, 4829–4836.

Amer, R., Kusky, T.M., Ghulam, A., 2010. Lithological mapping in the central eastern desert of Egypt using ASTER data. J. Afr. Earth Sci. 56 (2–3), 75–82.

Avé Lallemant, H., Guth, L.R., 1990. Role of extensional tectonics in exhumation of eclogites and blueschists in an oblique subduction setting: Northeastern Venezuela. Geology 18, 950–953.

Avigad, D., 1992. Exhumation of crossite bearing rocks in the Dora Maira massif western Alps Italy. Geology 20, 947–950.

Azizi, H., Rsaouli, A.A., Babaei, K., 2007. Using SWIR bands form ASTER for discrimination of hydrothermal altered minerals in the northwest of Iran (Sc-Sanandaj City); a key for exploration of copper and gold mineralization. Res. J. Appl. Sci. 2 (6), 763–768.

Bedell, R.L., 2001. Geological mapping with ASTER satellite: new global satellite data that is a significant leap in remote sensing geologic and alteration mapping. Geol. Soc. Nevada 33, 329–334.

Bedini, E., 2011. Mineral mapping in the Kap Simpson complex, central East Greenland, using HyMap and ASTER remote sensing data. Adv. Space Res. 47, 60–73.

Blom, R.G., Abrams, M.J., Adams, H.G., 1980. Spectral reflectance and discrimination of plutonic rocks in the 0.45–2.45 μm region. J. Geophys. Res. 85, 2638–2648.

Boardman, J.W., Kruse, F.A., 1994. Automated spectral analysis: a geological example using AVIRIS data, north grapevine mountains, Nevada. In: Proceedings, ERIM Tenth Thematic Conference on Geologic Remote Sensing. Environmental Research Institute of Michigan, Ann Arbor, MI I-407-I-418.

Chabrillat, S., Goetz, A.H., 2006. Remote sensing of expansive soils: use of hyperspectral methodology for clay mapping and hazard assessment. In: Ali Al-Rawas, A., Goosen, M.F.A. (Eds.), Expansive Soils: Recent Advances in Characterization and Treatment. Taylor & Francis, pp. 187–209.

Chen, J.Y., Reed, I.S., 1987. A detection algorithm for optical targets in clutter. IEEE Trans. Aerosp. Electron. Syst. AES-23 (1), 46–59.

Clark, R.N., King, T.V.V., Klejwa, M., Swayze, G.A., Vergo, N., 1990. High spectral resolution reflectance spectroscopy of minerals. J. Geophys. Res. 95, 12653–12680.

Clénet, H., Ceuleneer, G., Pinet, P., Abily, B., Daydou, Y., Harris, E., Amri, I., Dantas, C., 2010. Thick sections of layered ultramafic cumulates in the Oman ophiolite revealed by an airborne hyperspectral survey: petrogenesis and relationship to mantle diapirism. Lithos 114, 265–281.

Cloos, M., 1986. Blueschists in the Franciscan complex of California: petrotectonic constraints on uplift mechanisms. In: Evans, B.W., Brown, E.H. (Eds.), Blueschists and Eclogites, vol. 164. Geological Society of America Memoir, pp. 77–93.

Combe, J.P., Launeau, P., Pinet, P., Despan, D., Harris, E., Ceuleneer, G., Sotin, C., 2006. Mapping of an ophiolite complex by high-resolution visible-infrared spectrometry. Geochem. Geophys. Geosyst. 7 (8), 1–11.

Congalton, R.G., 1991. A review of assessing the accuracy of classifications of remotely sensed data. Remote Sens. Environ. 37 (1), 35–46.

Corrie, R.K., Ninomiya, Y., Aitchison, J.C., 2010. Applying advanced spaceborne thermal emission and reflection radiometer (ASTER) spectral indices for geological mapping and mineral identification on the Tibetan Plateau. In: International Archives of the Photogrammetry, Remote Sensing and Spatial Information Science, vol. XXXVIII, Part 8, Kyoto Japan 2010, pp. 464–469.

Crósta, A.P., Filho, C.R.D.S., 2003. Searching for gold with ASTER. Earth Obs. Mag. 12 (5), 38–41.

Crósta, A.P., Moore, M.J., 1989. Enhancement of landsat thematic mapper imagery for residual soil mapping in SW Minas Gerais State Brazil: a prospecting case history in greenstone belt terrain. In: 9th Thematic Conference on Remote Sensing for Exploration Geology. Environmental Research Institute of Michigan, Ann Arbor, pp. 1173–1187.

Crosta, A.P., Sabine, C., Taranik, J.V., 1998. Hydrothermal alteration mapping at Bodie, California, using AVIRIS hyperspectral data. Remote Sens. Environ. 65, 309–319.

Davy, P., Gillet, P., 1986. The stacking of thrust slices in collision zones and its thermal consequences. Tectonics 5, 913–929.

Dobretsov, N.L., 1991. Blueschists and eclogites: a possible plate tectonic mechanism for their emplacement from the upper mantle. Tectonophysics 186, 253–268.

Draper, G., Bone, R., 1981. Denudation rates, thermal evolution, and preservation of blueschist terrains. J. Geol. 89, 601–613.

El Janati, M., Soulaimani, A., Admou, H., Youbi, N., Hafid, A., Hefferan, K.P., 2014. Application of ASTER remote sensing data to geological mapping of basement domains in arid regions: a case study from the central Anti-Atlas, Iguerda inlier, Morocco. Arab. J. Geosci. 7, 2407–2422.

El-Shazly, A.K., 1994. Petrology of lawsonite-, pumpellyite- and sodic amphibole-bearing metabasites from northeast Oman. J. Metamorph. Geol. 12, 23–48.

El-Shazly, A.K., 1995. Petrology of Fe–Mg–carpholite-bearing metasediments from NE Oman. J. Metamorph. Geol. 13, 379–396.

El-Shazly, A.K., Coleman, R.G., 1990. Metamorphism in the Oman mountains in relation to Semail ophiolite emplacement. In: Robertson, A.F.H., Searle, M.P., Ries, A.C. (Eds.), The Geology and Tectonics of the Oman Region, vol. 49. Geological Society of London Special Publication, pp. 473–494.

El-Shazly, A.K., Lanphere, M.A., 1992. Two high-pressure metamorphic events in NE Oman: evidence from 40Ar/39Ar dating and petrological data. J. Geol. 100, 731–751.

El-Shazly, A.K., Coleman, R.G., Liou, J.G., 1990. Eclogites and blueschists from Northeastern Oman: petrology and P–T evolution. J. Petrol. 31, 629–666.

El-Shazly, A.K., Worthing, M.A., Jayawardane, J., Varne, R., 1994. Geochemistry of metamorphosed mafic rocks from Saih Hatat: pre-obduction history of NE Oman. J. Geol. Soc. 151, 999–1016.

El-Shazly, A.K., Worthing, Liou, J.G., 1997. Interlayered eclogites, blueschists and epidote amphibolites from NE Oman: a record of protolith compositional control and limited fluid infiltration. J. Petrol. 38, 1461–1487.

El-Shazly, A.K., Broker, W., Hacker, B., Calvert, A., 2001. Formation and exhumation of blueschists and eclogites from NE Oman: new perspectives from Rb–Sr and 40Ar/39Ar dating. J. Metamorph. Geol. 19, 233–248.

Ernst, W.G., 1988. Tectonic history of subduction zones inferred from retrograde blueschist *P–T* paths. Geology 16, 1081–1084.

Ferrier, G., White, K., Griffiths, G., Bryant, R., 2002. The mapping of hydrothermal alteration zones on the island of Lesvos, Greece using an integrated remote sensing dataset. Int. J. Remote Sens. 23, 341–356.

Fujisada, H., 1995. Design and performance of ASTER instrument. Proc. SPIE Int. Soc. Opt. Eng. 2583, 16–25.

Gabr, S., Ghulam, A., Kusky, T., 2010. Detecting areas of high-potential gold mineralization using ASTER data. Ore Geol. Rev. 38, 59–69.

Gad, S., Kusky, T., 2006. Lithological mapping in the eastern desert of Egypt, the Barramiya area, using landsat thematic mapper (TM). J. Afr. Earth Sci. 44, 196–202.

Gad, S., Kusky, T.M., 2007. ASTER spectral ratioing for lithological mapping in the Arabian–Nubian shield, the neoproterozoic Wadi Kid area, Sinai, Egypt. Gondwana Res. 11 (3), 326–335.

Galvao, L.S., Filho, R.A., Vitorello, C., 2005. Spectral discrimination of hydrothermal altered materials using ASTER Short_wave infrared bands, evaluation in a tropical Savannah environment. Int. J. Appl. Earth Obs. Geoinf. 7, 107–114.

Gillespie, A.R., Kahle, A.B., Walker, R.E., 1986. Color enhancement of highly correlated images. 1. Decorrelation and HSI contrast stretches. Remote Sens. Environ. 20, 209–735.

Goffé, B., Michard, A., Kienast, J.R., Le Mer, O., 1988. A case of obduction related high *P* low *T* metamorphism in upper crustal nappes, Arabian continental margin, Oman: *P–T* paths and kinematic interpretation. Tectonophysics 151, 363–386.

Gray, D.R., Gregory, R.T., Miller, J.M., 2000. A new structural profile along the Muscat-Ibra transect, Oman: implications for emplacement of the Semail ophiolite. Geol. Soc. Am. Special Paper 349, 513–523.

Please cite this article in press as: Rajendran, S., Nasir, S. Mapping of high pressure metamorphics in the As Sifah region, NE Oman using ASTER data. Adv. Space Res. (2014), http://dx.doi.org/10.1016/j.asr.2014.11.026

Gray, D.R., Miller, J.M., Gregory, R.T., 2005. Strain state and kinematic evolution of a fold-nappe beneath the Samail ophiolite, Oman. J. Struct. Geol. 27, 1986–2007.

Green, A.A., Berman, M., Switzer, P., Craig, M.D., 1988. A transform for ordering multispectral data in terms of image quality with implications for noise removal. IEEE Trans. Geosci. Remote Sens. 26 (1), 65–74.

Gregory, R.T., Gray, D.R., Miller, J.M., 1998. Tectonics of the Arabian margin associated with the emplacement of the Oman margin along the Ibra transect: new evidence from northeast Saih Hatat. Tectonics 17, 657–670.

Hanna, S., 1990. The alpine deformation of the central Oman mountains. In: Robertson, A.F.H., Searle, M.P., Ries, A.C. (Eds.), The Geology and Tectonics of the Oman Region, vol. 49. Geological Society, London, pp. 341–359.

Hecker, C.A., van der Meijde, M., van der Werff, H.M.A., van der Meer, F.D., 2008. Assessing the influence of reference spectra on synthetic SAM classification results. IEEE Trans. Geosci. Remote Sens. 46 (12), 4162–4172.

Hosseinjani, M., Tangestani, M.H., 2011. Mapping alteration minerals using sub-pixel unmixing of ASTER data in the Sarduiyeh area, SE Kerman, Iran. Int. J. Digital Earth 4 (6), 487–504.

Hunt, G.R., 1977. Spectral signatures of particulate minerals in the visible and near infrared. Geophysics 42, 501–503.

Hunt, G.R., 1979. Near-infrared (1.3–2.4) spectra of alteration minerals – potential for use in remote sensing. Geophysics 44 (12), 1974–1986.

Hunt, G.R., Ashley, P., 1979. Spectra of altered rocks in the visible and near infrared. Econ. Geol. 74, 1613–1629.

Hunt, G.R., Salisbury, J.W., 1970. Visible and near infrared spectra of minerals and rocks: I. Silicate minerals. Mod. Geol. 1, 283–300.

Hunt, G.R., Salisbury, J.W., Lenhoff, C.J., 1973. Visible and near-infrared spectra of minerals and rocks. VI. Additional silicates. Mod. Geol. 4, 85–106.

Hunt, G.R., Salisbury, J.W., Lenhoff, C.J., 1974. Visible and near-infrared spectra of minerals and rocks. IX. Basic and ultrabasic igneous rocks. Mod. Geol. 5, 15–22.

Jia, X., Richards, A., 1994. Efficient maximum likelihood classification for imaging spectrometer data sets. IEEE Trans. Geosci. Remote Sens. 32 (2), 274–281.

Khan, S.D., Glenn, N., 2006. New strike slip faults and litho-units mapped in Chitral (N. Pakistan) using field and ASTER data yield regionally significant results. Int. J. Remote Sens. 27, 4495–4512.

Khan, S.D., Mahmood, K., 2008. The application of remote sensing techniques to the study of ophiolites. Earth Sci. Rev. 89, 135–143.

Khan, S.D., Mahmood, K., Casey, J.F., 2007. Mapping of Muslim Bagh ophiolite (Pakistan) using new remote sensing and field data. J. Asian Earth Sci. 30, 333–343.

Kruse, F.A., Lefkoff, A.B., Boardman, J.B., Heidebreicht, K.B., Shapiro, A.T., Barloon, P.J., 1993. The spectral image processing system (SIPS)—interactive visualization and analysis of imaging spectrometer data. Remote Sens. Environ. 44, 145–163.

Kruse, F.A., Boardman, J.W., Hunnington, J.F., 2003. Comparison of airborne hyperspectral data and EO-1 hyperion for mineral mapping. IEEE Trans. Geosci. Remote Sens. 41 (6), 1388–1400.

Kusky, T.M., Ramadan, T., 2002. Structural controls on Neoproterozoic mineralization in the SE Desert, Egypt: an integrated field, landsat TM, and SIR C/X approach. J. Afr. Earth Sci. 35, 107–121.

Le Métour, J., de Gramont, X., Villey, M., 1986. Geological map of Masqat and Quryat and accompanying notes. Scale 1:100,000, Ministry of Petroleum and Minerals, Sultanate of Oman.

Le Métour, J., Rabu, D., Tegyey, M., Bechennec, F., Beurrier, M., Villey, M., 1990. Subduction and obduction: two stages in the Eo-Alpine tectonometamorphic evolution of the Oman mountains. Geol. Soc. Lond. Special Publ. 49, 327–339.

Lippard, S.J., Shelton, A.W., Gass, I.G., 1986. The ophiolite of northern Oman, Geological Society of London Memoir 11, Blackwell Scientific Publications, Oxford, pages 178.

Liu, F., Wu, X., Sun, H., Guo, Y., 2007. Alteration information extraction by applying synthesis processing techniques to Landsat ETM+ data: case study of Zhaoyuan Gold Mines, Shandong Province, China. J. China Univ. Geosci. 18, 72–76.

Loughlin, W.P., 1991. Principal component analysis for alteration mapping. Photogramm. Eng. Remote Sens. 57, 1163–1169.

Mann, P., Gordon, M.B., 1996. Tectonic uplift and exhumation of blueschist belts along transpressional strike slip fault zones. In: Subduction: Top to Bottom, vol. 96, American Geophysical Union Monograph, pp. 143–154.

Mars, J.C., Rowan, L.C., 2010. Spectral assessment of new ASTER SWIR surface reflectance data products for spectroscopic mapping of rocks and minerals. Remote Sens. Environ. 114, 2011–2025.

Massonne, H.J., Opitz, J., Theye, T., Nasir, S., 2013. Evolution of a very deeply subducted metasediment from As Sifah, northeastern coast of Oman. Lithos 156–159, 171–185.

Matthews, J.P., Jones, A.S.G., 1992. Mapping the Xigaze (Tibet) ophiolite complex with landsat thematic mapper data. J. Himalayan Geol. 3, 97–101.

Michard, A., Bouchez, J.-L., Ouazzani-Touhami, M., 1984. Obduction related planar and linear fabrics in Oman. J. Struct. Geol. 6, 39–49.

Miller, J.M., Gray, D.R., Gregory, R.T., 1998. Exhumation of high-pressure rocks in northeastern Oman. Geology 26, 235–238.

Miller, J.M., Gregory, R.T., Gray, D.R., Foster, D.A., 1999. Geological and geochronological constraints on the exhumation of a high-pressure metamorphic terrane, Oman. In: Ring, U. et al. (Eds.), Exhumation Processes: Normal Faulting, Ductile Flow and Erosion, vol. 154. Geological Society Special Publication, pp. 241–260.

Miller, J.M., Gray, D.R., Gregory, R.T., 2002. Geometry and significance of internal windows and regional isoclinal folds in Northeast Saih Hatat, Sultanate of Oman. J. Struct. Geol. 24, 359–386.

Ministry of Petroleum and Minerals, 1986. Directorate General of Minerals, Sultanate of Oman. Geological map of Masqat and Quryat, sheets NF40-4A, NF40-4D and explanatory notes. Scale 1:100,000.

Ninomiya, Y., 2002. Mapping quartz, carbonate minerals and mafic–ultramafic rocks using remotely sensed multispectral thermal infrared ASTER data. Proc. SPIE 4710, 191–202.

Ninomiya, Y., Fu, B., Cudahy, T.J., 2005. Detecting lithology with advanced spaceborne thermal emission and reflection radiometer (ASTER) multispectral thermal infrared "radiance-at-sensor" data. Remote Sens. Environ. 99, 127–139.

Ninomiya, Y., Fu, B., Cudhy, T.J., 2006. Corrigendum to "detecting lithology with advanced spaceborne thermal emission and refection radiometer (ASTER) multispectral thermal infrared 'radiance-at-sensor' data". Remote Sens. Environ. 101, 567.

Pearce, J.A., Alabaster, T., Shelton, A.W., Searle, M.P., 1981. The Oman ophiolite as a Cretaceous arc-basin complex, evidence and implications. In: Vine, F.J., Smith, A.G. (Eds.), Extensional Tectonics Associated with Convergent Plate Boundaries. Philosophical Transactions of the Royal Society London, 300A, 1454, pp. 299–317.

Philip, G., Ravindran, K.V., Mathew, J., 2003. Mapping the Nidar ophiolite complex of the Indus suture zone, Northwestern-Trans Himalaya using IRS-1C/1D data. Int. J. Remote Sens. 24, 4979–4994.

Platt, J.P., 1986. Dynamics of orogenic wedges and the uplift of high-pressure metamorphic rocks. Geol. Soc. Am. Bull. 97, 1037–1053.

Rajendran, S., Nasir, S., 2013a. Mapping of manganese potential lithology using ASTER satellite data in parts of sultanate of Oman. Int. J. Geosci. Geomatics 1 (2), 92–101.

Rajendran, S., Nasir, S., 2013b. ASTER spectral analysis of ultramafic lamprophyres (carbonatites and aillikites) within the Batain nappe, northeastern margin of Oman—a proposal developed for spectral absorption. Int. J. Remote Sens. 34 (8), 2763–2795.

Rajendran, S., Nasir, S., 2014a. Hydrothermal altered serpentinized zone and a study of Ni-magnesioferrite–magnetite–awaruite occurrences in Wadi Hibi, Northern Oman Mountain: discrimination through ASTER mapping. Ore Geol. Rev. 62, 211–226.

Rajendran, S., Nasir, S., 2014b. ASTER spectral sensitivity of carbonate rocks – study in Sultanate of Oman. Adv. Space Res. 53, 656–673.

Please cite this article in press as: Rajendran, S., Nasir, S. Mapping of high pressure metamorphics in the As Sifah region, NE Oman using ASTER data. Adv. Space Res. (2014), http://dx.doi.org/10.1016/j.asr.2014.11.026

Rajendran, S., Nasir, S., 2014c. ASTER mapping of limestone formations and study of caves, springs and depressions in parts of Sultanate of Oman. Environ. Earth Sci. 71, 133–146.

Rajendran, S., Hersi, O.S., Al-Harthy, A.R., Al-Wardi, M., ElGhali, M., Al-Abri, Amani Humaid, 2011a. Capability of Advanced spaceborne thermal emission and reflection radiometer (ASTER) on discrimination of carbonates and associated rocks and mineral identification of eastern mountain region (Saih Hatat Window) of Sultanate of Oman. Carbonates Evaporites 26, 351–364.

Rajendran, S., Thirunavukkarasu, A., Balamurugan, G., Shankar, K., 2011b. Discrimination of iron ore deposits of granulite terrain of Southern Peninsular India using ASTER data. J. Asian Earth Sci. 41, 99–106.

Rajendran, S., Al-Khirbash, S., Pracejus, B., Nasir, S., Al-Abri, Amani Humaid, Kusky, T.M., Ghulam, A., 2012. ASTER detection of chromite bearing mineralized zones in Semail ophiolite massifs of the northern Oman mountain: exploration strategy. Ore Geol. Rev. 44, 121–135.

Rajendran, S., Nasir, S., Kusky, T.M., Ghulam, A., Gabr, S., Elghali, M., 2013. Detection of hydrothermal mineralized zones associated with Listwaenites rocks in the Central Oman using ASTER data. Ore Geol. Rev. 53, 470–488.

Rajendran, S., Nasir, S., Kusky, T.M., Al-Khirbash, S., 2014. Remote sensing based approach for mapping of CO_2 sequestered regions in Semail ophiolite massifs of the Sultanate of Oman. Earth Sci. Rev. 135, 122–140.

Richards, J.A., Jia, X., 2006. Remote Sensing Digital Image Analysis. Springer, Berlin.

Richards, J.A., Xiuping, J., 1998. Remote Sensing Digital Image Analysis, third ed. Springer, Berlin, 363.

Rockwell, B.W., Hofstra, A.H., 2008. Identification of quartz and carbonate minerals across northern Nevada using ASTER thermal infrared emissivity data implications for geologic mapping and mineral resource investigations in well-studied and frontier areas. Geosphere 4 (1), 218–246.

Rokos, D., Argialas, D., Mavrantza, R., St-Seymour, K., Vamvoukakis, C., Kouli, M., Lamera, S., Paraskevas, H., Karfakis, I., Denes, G., 2000. Structural mapping and analysis for a preliminary investigation of possible gold mineralization by using remote sensing and geochemical techniques in a GIS environment: study area: island of Lesvos, Aegean Sea, Hellas. Nat. Resour. Res. 9, 277–293.

Rothery, D.A., 1987. The role of Landsat multispectral scanner (MSS) imagery in mapping the Oman ophiolite. J. Geol. Soc. Lond. 144, 587–597.

Rowan, L.C., Mars, J.C., 2003. Lithologic mapping in the Mountain Pass area, California using advanced spaceborne thermal emission and reflection radiometer (ASTER) data. Remote Sens. Environ. 84 (3), 350–366.

Rowan, L., Hook, S.J., Abrams, M.J., Mars, J.C., 2003. Mapping hydrothermally altered rocks at Cuprite, Nevada, using the advanced spaceborne thermal emission and reflection radiometer (ASTER), a new satellite-imaging system. Econ. Geol. Bull. Soc. Econ. Geol. 98 (5), 1019–1027.

Rowan, I.C., Mars, J.C., Simpson, C.J., 2005. Lithologic mapping of the Mordor, NT, Australia ultramafic complex by using the advanced spaceborne thermal emission and reflection radiometer (ASTER). Remote Sens. Environ. 99, 105–116.

Rown, L.C., Schmidt, R.G., Mars, J.C., 2006. Distribution of hydrothermally altered rocks in Reko Diq, Pakistan mineralized area based on spectra analysis of ASTER data. Remote Sens. Environ. 104, 74–87.

Sabol, D.E., Adams, J.B., Smith, M.O., 1992. Quantitative sub-pixel spectral detection of targets in multispectral images. J. Geophys. Res. 97, 2659–2672.

Searle, M.P., 1985. Sequence of thrusting and origin of culminations in the northern and central Oman mountains. J. Struct. Geol. 7, 129–143.

Searle, M.P., Cox, J.S., 1999. Tectonic setting, origin and obduction of the Oman ophiolite. Geol. Soc. Am. Bull. 111, 104–122.

Searle, M.P., Cox, J.S., 2002. Subduction zone metamorphism during formation and emplacement of the Semail ophiolite in the Oman mountains. Geol. Mag. 139, 241–255.

Searle, M.P., Malpas, J., 1980. The structure and metamorphism of rocks beneath the Semail ophiolite of Oman and their significance in ophiolite obduction. Trans. R. Soc. Edinburgh Earth Sci. 71, 247–262.

Searle, M.P., Malpas, J., 1982. Petrochemistry and origin of sub-ophiolite metamorphic and related rocks in the Oman mountains. J. Geol. Soc. 139, 235–248.

Searle, M.P., Waters, D.J., Martin, H.N., Rex, D.C., 1994. Structure and metamorphism of blueschist–eclogite facies rocks from the northeastern Oman mountains. J. Geol. Soc. 151, 555–576.

Searle, M.P., Warren, C.J., Waters, D.J., Parrish, R.R., 2004. Structural evolution, metamorphism and restoration of the Arabian continental margin, Saih Hatat region, Oman mountains. J. Struct. Geol., 451–473.

Sultan, M., Arvidson, R.E., 1986. Mapping of serpentinites in the eastern desert of Egypt by using landsat thematic mapper data. J. Geol. 14, 995–999.

Sultan, M., Arvidson, R.E., Sturchio, N.C., Guinness, E.A., 1987. Lithologic mapping in arid regions with landsat thematic mapper data: Meatiq dome, Egypt. Geol. Soc. Am. Bull. 99, 748–762.

Tangestani, M.H., Mazhari, N., Agar, B., Moore, F., 2008. Evaluating advanced spaceborne thermal emission and reflection radiometer (ASTER) data for alteration zone enhancement in a semiarid area, northern Shahr-e-Babak, SE Iran. Int. J. Remote Sens. 29, 2833–2850.

Tangestani, M.H., Jaffari, L., Vincent, R.K., Maruthi Sridhar, B.B., 2011. Spectral characterization and ASTER-based lithological mapping of an ophiolite complex: a case study from Neyriz ophiolite, SW Iran. Remote Sens. Environ. 115, 2243–2254.

Van Der Meer, F., 1995. Spectral unmixing of landsat thematic mapper data. Int. J. Remote Sens. 16, 3189–3194.

Warren, C.J., Waters, D.J., 2006. Oxidized eclogites and garnet blueschists from Oman: *P–T* path modelling in the NCFMASHO system. J. Metamorph. Geol. 24, 783–802.

Warren, C.J., Parrish, R.R., Searle, M.P., Waters, D.J., 2003. Dating the subduction of the Arabian continental margin beneath the Semail ophiolite, Oman. Waters, D.J., Martin, H.N., 1993. Geobarometry in phengite-bearing eclogites. Terra Abstracts, vol. 5, pp. 410–411.

Wendt, A.S., D'Arco, P., Goffé, B., Oberhänsli, R., 1993. Radial cracks around a-quartz inclusions in almandine: constraints on the metamorphic history of the Oman mountains. Earth Planet. Sci. Lett. 114, 449–461.

Xu, Z., Zhao, H., 2008. A new spectral unmixing algorithm based on spectral information divergence. Proc. SPIE 7127 (7), 712–726.

Yamato, P., Agard, P., Goffé, B., De Andrade, V., Vidal, O., Jolivet, L., 2007. New, high precision P–T estimates for Oman blueschists: implications for obduction, nappe stacking and exhumation processes. J. Metamorph. Geol. 25, 657–682.

Yuhas, R.H., Goetz, A.F.H., Boardman, J.W., 1992. Discrimination among semi-arid landscape endmembers using the spectral angle mapper (SAM) algorithm. JPL Publ. 4 (92–41), 147–149.

Zhang, X., Pazner, M., Duke, N., 2007. Lithologic and mineral information extraction for gold exploration using ASTER data in the south Chocolate Mountains (California). Photogramm. Remote Sens. 62, 271–282.

Please cite this article in press as: Rajendran, S., Nasir, S. Mapping of high pressure metamorphics in the As Sifah region, NE Oman using ASTER data. Adv. Space Res. (2014), http://dx.doi.org/10.1016/j.asr.2014.11.026